Applied Ocean Research 97 (2020) 102042

Contents lists available at ScienceDirect

Applied Ocean Research

journal homepage: www.elsevier.com/locate/apor

Two-dimensional experimental and numerical investigations of parallel perforated plates in oscillating and orbital flows

Fredrik Mentzoni*, Trygve Kristiansen

Department of Marine Technology, Norwegian University of Science and Technology, Trondheim, NO-7491, Norway

ARTICLE INFO

Keywords:
Perforated plate
Added mass
Damping
Computational fluid dynamics
Experimental study

ABSTRACT

The hydrodynamic loads on two-dimensional perforated plates are investigated experimentally and numerically. Two parallel plate configurations, consisting of an upper perforated plate and a lower perforated plate, are studied. The difference between the two configurations is the gap distance between the upper and the lower plates, being 0.14 and 0.29 times the width of the plates. Comparisons are made between forced oscillation experiments and numerical simulations of oscillating and orbital flow conditions. The Keulegan–Carpenter (KC) number and period of oscillation are varied. Added mass and damping coefficients are presented. The coefficients are highly KC number dependent. There is in general small dependence on the period of oscillation. The force coefficients are in general somewhat larger for the largest gap distance. The hydrodynamic force on both configurations is dominated by damping. We find in general good agreement between the experimental and numerical results.

Interaction effects between the plates of the parallel configurations are studied. The interaction effects increase with increasing KC number and depend on the distance between the two plates. Compared to the force on one single perforated plate, interaction effects influence the phase and magnitude of the force on the upper and lower plates in the parallel configurations. A reduction in hydrodynamic force, compared to that of one single plate, is found for both plates, in particular for the downstream plate.

1. Introduction

1.1. Structure

This is the second part of a study on the hydrodynamic loads on perforated plates in waves and oscillating and orbital flows. The focus in the second part is on the hydrodynamic interaction of two parallel perforated plates in oscillating and orbital flow. The first part of the study is on the hydrodynamic forces of single perforated plates in waves compared to oscillating and orbital flows [1]. The two parts are closely related. However, the introduction, theory and method sections are included in both parts, such that they can be read separately.

This part of the study is organized in six main sections. The first covers the present introduction with motivational background. In Sections 2–4 we present definitions of hydrodynamic coefficients, the experimental setup and the numerical methods. Results are presented and discussed in Section 5. Finally, conclusions are drawn in the last section.

1.2. Background

Safe and cost-efficient marine operations are essential for the development of subsea fields. Typically, the structures and modules of subsea fields are lifted by cranes on vessels, lowered through the water, and installed on the seabed. Operations include installation of new modules, as well as maintenance and modification of existing ones.

There is an industrial demand to perform such operations on an all-year basis. The goal is to increase the operational weather window, and thereby decrease the risk of costly delays. All-year operability implies more demanding conditions, and must be achieved together with, and not at the expense of, safe operations. Unsafe conditions can lead to drop accidents, risk for personnel and damages to the structure, crane or vessel. Consequently, there is a need for accurate estimates of the hydrodynamic forces that subsea structures are exposed to during the lifting and lowering phases in harsh environments.

Perforated plates share direct similarities with main structural elements found on complex subsea modules, e.g. hatch covers and mudmats. In particular, the perforated plate model is relevant when the structure parts are relatively wide compared to their thickness, and

* Corresponding author.
E-mail address: fredrik.mentzoni@ntnu.no (F. Mentzoni).

https://doi.org/10.1016/j.apor.2019.102042
Received 16 August 2019; Received in revised form 19 November 2019; Accepted 20 December 2019
Available online 09 February 2020

consist of many openings. The hydrodynamic forces on these structural components are likely to be dominant for the total force on the modules. In previous experimental studies within the same project, simplified subsea structures consisting of perforated plates in combination with other structural components has been studied. The total hydrodynamic force on these simplified subsea structures are typically dominated by the perforated plates; for example, we found almost no difference in the hydrodynamic coefficients of two perforated plates in parallel compared to two perforated plates in parallel with five cylinders in between [2]. Later, we developed a numerical tool for estimating the hydrodynamic forces on two-dimensional perforated structures [3], and utilized the tool to study the importance of perforation ratio and amplitude of motion on the hydrodynamic forces of perforated plates [4]. Furthermore, various mudmat configurations were investigated experimentally and numerically in a separate study [5].

In addition to protection structures found on subsea modules, perforated plates are relevant in several industrial applications; perforated structures are used as heave plates, wave absorbers, swash bulkheads and other damping plates. Consequently, there has been a great deal of work concerned with the hydrodynamics of perforated structures. An extensive review was given by Molin in 2011 [6]. In the review, Molin presents the background for his semi-analytical method for calculating the hydrodynamic coefficients of perforated structures. The semi-analytical method is based on the assumption of a quadratic pressure-drop condition for the flow through the openings of the perforated structure, combined with potential flow conditions in the fluid domain. A consequence of the quadratic pressure drop condition is that the hydrodynamic coefficients of perforated structures are functions of the amplitude of motion. The method has been applied to various problems and several cases are presented and discussed, including the relevance for protection structures of subsea modules.

Among other relevant studies are the works by Sandvik et al. [7], Tao and Dray [8], An and Faltinsen [9], Li et al. [10], and Tian et al. [11]. These studies agree that experimentally obtained hydrodynamic coefficients of perforated plates depend on both the KC number and the perforation ratio, τ. In the study by Sandvik et al. [7], experimental investigations of five hatch cover models with perforation ratios $\tau = 0.15$, $\tau = 0.25$, $\tau = 0.27$, $\tau = 0.38$ and $\tau = 0.47$ were performed for $0.1 < \mathrm{KC} < 1.7$. Tao and Dray [8] performed experiments for $0.2 \leq \mathrm{KC} \leq 1.2$ of four similar circular disks with varying perforation ratios, $\tau = 0$, $\tau = 0.05$, $\tau = 0.1$ and $\tau = 0.2$. An and Faltinsen [9] investigated two similar perforated rectangular plates of $\tau = 0.08$ and $\tau = 0.16$ for $0.17 \leq \mathrm{KC} \leq 1.7$. The experimental study by Li et al. [10] included perforated rectangular plates of $\tau = 0.01$, $\tau = 0.05$ and $\tau = 0.10$ for $0.2 \leq \mathrm{KC} \leq 1.0$. The perforated disks in the study by Tian et al. [11] have perforation ratios $\tau = 0.05$, $\tau = 0.10$ and $\tau = 0.20$ and are tested for $0.15 \leq \mathrm{KC} \leq 3.15$. The following two observations are highlighted in these studies: 1) For a given perforation ratio, increasing the KC number increases, in general, the hydrodynamic coefficients. 2) For a given KC number, increasing the perforation ratio decreases, in general, the hydrodynamic coefficients. An exception to 2) is reported by Tao and Dray [8], where the damping coefficients for small KC numbers for (relatively dense) perforated plates can be higher than corresponding solid plates. This has also been found in studies using semi-analytical [12] and numerical [4] methods.

Of particular interest for the study of parallel perforated plates is the study by Tian et al. [11], which included multiple disk configurations. Five different gap distances were tested for two parallel disks, with a ratio of the distance between the two disks to the disk diameter ranging from 0.075 to 0.755. They found that the hydrodynamic coefficients, in general, increased with increasing gap distance between the disks. However, none of the parallel configurations had larger coefficients than multiplying that of a single disk by two. Furthermore, it was found that when the gap distance was very small, the coefficients of two parallel disks could be smaller than those of one disk. According to Tian et al., this is because the hydrodynamics of two parallel plates with a very small gap is similar to that of a single thick plate, which for large KC numbers can have hydrodynamic coefficients smaller than that of thin plates. The study by Tian et al. includes both perforated and solid disks, however, the multiple disk configurations consist of solid disks only. Moreover, the studies by Tao et al. [13], and Sudhakar and Nallayarasu [14] included investigations of gap distance for stacked heave plates, but the plates studied were not perforated.

There are many studies on single perforated plates, however, for the case of two parallel perforated plates, which can be particularly relevant for subsea modules, there exists, to the authors' knowledge, not much published work. Multiplate configurations of solid and perforated plates ($\tau = 0.05$) were investigated by Li et al. [10], but these configurations consisted of three plates. Different gap distances between the plates were tested. When the plates were placed relatively far from each other, the hydrodynamic coefficients were similar to three times that of a single plate, whereas when the plates were placed closer to each other, interaction effects between the plates reduced the hydrodynamic coefficients. Several studies have looked at progressive wave absorbers, which consists of series of vertical perforated plates, and thus share some features with parallel perforated plates, e.g. [15]. More relevant for the present study is the work by Molin [12], in which arrays of stacked porous disks were studied in oscillating flow. Using his semi-analytical method, Molin studied the effect of varying the distance between the disks. The added mass and damping coefficients of the disks were presented in terms of a porous KC number. The coefficients were found to depend on the distance between the disks. The increase in damping was relatively small when increasing the relative distance between the plates two or five times, and thus, many disks placed closely together would yield the largest damping of the system as a whole. However, the effect of flow separation at the plate-ends was not accounted for. In later studies, Molin and several other authors have highlighted the importance of flow separation at the plate-ends [4,6,7,9,10,16], in particular when the perforation ratio is small and/or the KC number is large.

The aim of the present study is to increase our understanding of the hydrodynamic behavior and forces on perforated structures of subsea modules in waves. In this second part of the study, parallel perforated plates, consisting of numerous sharp-edged holes, with special attention on the interaction effects between the upper and the lower plates, are studied. Experimental and numerical investigations of the structures in oscillating flow conditions in infinite fluid domains are performed. Additionally, orbital flow conditions are studied numerically. In orbital flow, the horizontal and vertical velocity components vary harmonically in time, but has no spatial variations. Thus, orbital flow conditions may be regarded as a limiting case of a body submerged in waves, where the wave length is long compared to the model, and the model is deeply submerged, such that there is no interaction with a free surface. Consequently, orbital flow simulations may be regarded as a first step towards simulations in waves. Hydrodynamic forces and coefficients are presented for a range of Keulegan–Carpenter (KC) numbers and periods of oscillation. Moreover, we include flow visualizations from our numerical simulations to highlight important physical phenomena, in particular flow separation from the plate ends.

2. Hydrodynamic forces and coefficients

Two flow conditions are considered: 1) oscillating flow and 2) orbital flow. In oscillating flow, the horizontal velocity component is zero, whereas the vertical velocity component oscillates harmonically. Note that there is a difference between the oscillating flow experiments—in which the models are forced to oscillate in otherwise calm water—and the oscillating flow numerical simulations—in which the models are fixed and the ambient velocity, set on the boundaries of the numerical domains, oscillates. In orbital flow (only numerical), both the horizontal and vertical ambient velocities oscillate harmonically. Results are, typically, presented in terms of hydrodynamic force coefficients

(added mass and damping) as functions of the Keulegan–Carpenter (KC) number. The KC numbers are based on the amplitude of the velocity. In the following, the relevant parameters are presented.

The results of the present study are presented as functions of the Keulegan–Carpenter (KC) number. For oscillating and orbital flow conditions, this is taken as

$$\mathrm{KC} = \frac{WT}{D}, \tag{1}$$

with W being the amplitude of the first harmonic of the prescribed (numerical results) or measured (experimental results) velocity, T being the oscillation period and D the characteristic dimension of the structure (width of the plate).

Added mass and damping coefficients are extracted from the experiments. The models are forced to oscillate in otherwise calm water. The plates are horizontal, while the vertical force is measured. The measured hydrodynamic radiation force is decomposed into added mass and damping terms,

$$F = A\ddot{\eta} + B\dot{\eta} \tag{2}$$

with F being the measured net hydrodynamic force, A the added mass coefficient, $\ddot{\eta}$ the harmonically oscillating acceleration, B the damping coefficient and $\dot{\eta}$ the harmonically oscillating velocity. The measured force from corresponding tests without any model in the experimental rig is subtracted, time-step by time-step, in order to find the net hydrodynamic force on the models.

The added mass and damping coefficients are obtained by Fourier averaging,

$$A\int_{mT} \ddot{\eta}\ddot{\eta}\ dt + 0 = \int_{mT} F\ddot{\eta}\ dt, \tag{3}$$

$$0 + B\int_{mT} \dot{\eta}\dot{\eta}\ dt = \int_{mT} F\dot{\eta}\ dt. \tag{4}$$

Here m indicates a selected oscillation period. The forced oscillation experiments consist of 20 oscillation periods for each combination of period and amplitude. The first five periods gradually ramp the signal to its prescribed amplitude, then follows ten full cycles at the prescribed amplitude, before the signal is gradually ramped out to zero during the last five oscillations. The ramp is linear, hence the signal can be written

$$\eta = \begin{cases} \frac{t}{5T}\eta_a \sin\omega t; & 0 \le t < 5T, \\ \eta_a \sin\omega t; & 5T \le t < 15T, \\ (1 - \frac{t-15T}{5T})\eta_a \sin\omega t; & 15T \le t < 20T. \end{cases} \tag{5}$$

Here η_a is the prescribed amplitude. The mean of the oscillation cycles with the prescribed amplitude of motion, $5 < m < 15$, are used to calculate the coefficients. The variations during these 10 cycles is also investigated.

Results from the numerical simulations of oscillating and orbital flow are presented in a similar manner; coefficients and force amplitudes are based on the mean of the vertical force from the oscillation cycles with the prescribed amplitude of motion. In the numerical simulations, 30 cycles are simulated including two cycles of ramp-in of the signal. The mean of the last 25 oscillation cycles, $5 < m < 30$, are used to calculate the coefficients.

In the numerical simulations of oscillating and orbital flow, the discretized models are fixed and experience an ambient sinusoidally oscillating flow. Therefore, the total calculated force on the models consists of the hydrodynamic diffraction force and the Froude–Krylov force. In order to compare the experimental and numerical results, the Froude–Krylov force is subtracted, and the diffraction force is decomposed in a damping term, proportional to the ambient velocity, and an added mass term, proportional to the ambient acceleration, according to Eq. (2).

The results of the present study are presented in terms of dimensionless hydrodynamic coefficients and forces. The added mass and damping coefficients are made nondimensional by the corresponding analytical solid flat plate added mass,

$$A_0 = \rho\frac{\pi}{4}D^2L, \tag{6}$$

where ρ is the density and L is the length in the lateral direction of the structure. End plates are used in the experimental investigations to yield a near two-dimensional setup. Therefore, A_0 is taken as the two-dimensional analytical added mass times L. The numerical simulations are two-dimensional and Eq. (6) is used without the multiplication of L.

From Eqs. (2) and (6), an expression for the normalized hydrodynamic force can be obtained for the case of a harmonically oscillating plate velocity $w = W\sin\omega t$,

$$\frac{F}{\omega W A_0} = \sqrt{\left(\frac{A}{A_0}\right)^2 + \left(\frac{B}{\omega A_0}\right)^2}\ \sin(\omega t + \phi). \tag{7}$$

Here ϕ is the phase difference between the velocity and the normalized force.

3. Experiments

Forced oscillation experiments of two parallel perforated plate configurations are performed in a wave flume at the Marine technology center in Trondheim, Norway. The tank is approximately 13.5 m long and 0.60 m wide. A rig is placed in the middle of the tank. The rig consists of two acrylic glass plates, parallel to the tank walls, fastened to a wooden box on the top end, that is connected to a steel frame. The steel frame is connected to a 400 N force transducer connected to an actuator on the top. The acrylic glass plates act as end-plates, which yields a near two-dimensional setup. The gap between the acrylic glass plates and the tank walls are 9 mm. The tested models are installed through screw holes in the acrylic glass plates. Yellow putty is used to fill holes that are not used. The setup allows for testing a large range of structures in different orientations and placements, and has previously been used in experimental investigations of ideal perforated plates, cylinders, simplified mudmats and subsea structures [2,3,5].

A photo of the rig, with a structure consisting of two parallel perforated plates fastened inside the acrylic glass plates, is presented in Fig. 1.

A sketch of the experimental setup is presented in Fig. 2. The models are placed in the middle of the tank; the center of the model is 0.5 m from the free surface and the bottom of the tank, and approximately 6.5 m from the end walls of the wave flume. The water depth is $h = 1.0$ m. Parabolic beaches, to damp out radiated waves, are placed on both ends of the tank. The top of the beaches are set 2 mm below the free surface.

Two parallel plate configurations are experimentally investigated. We use the abbreviation 2P28 when referring to these configurations. Photos of the perforated plates of 2P28 are presented in Fig. 3; details are given in Table 1. The plates of 2P28 are equal in shape and size, both being $D = 420$ mm wide, $t = 3$mm thick, and $L = 0.57$ m long, such that they fit inside the acrylic glass plates of the experimental rig. The difference between the two configurations is the gap distance between the upper and lower plates. The gap distances are 60 mm (2P28_60) and 120 mm (2P28_120), which yields gap-to-width ratios of 0.14 (2P28_60) and 0.29 (2P28_120).

The perforation ratio of the perforated plates is $\tau = 0.28$. Each plate consists of approximately 10,000 equally distant circular holes of 3 mm diameter with 2 mm distance between the outer edge of each hole. Due to the extensive number of openings, and the large width-to-thickness ratio of $\frac{D}{t} = 140$, these perforated plates are close to ideal in the sense that they yield approximately zero added mass for KC → 0 [6]. However, two 20 mm aluminum profiles fitted along the length-span of the plates, used to increase the stiffness, as well as the fastening profiles

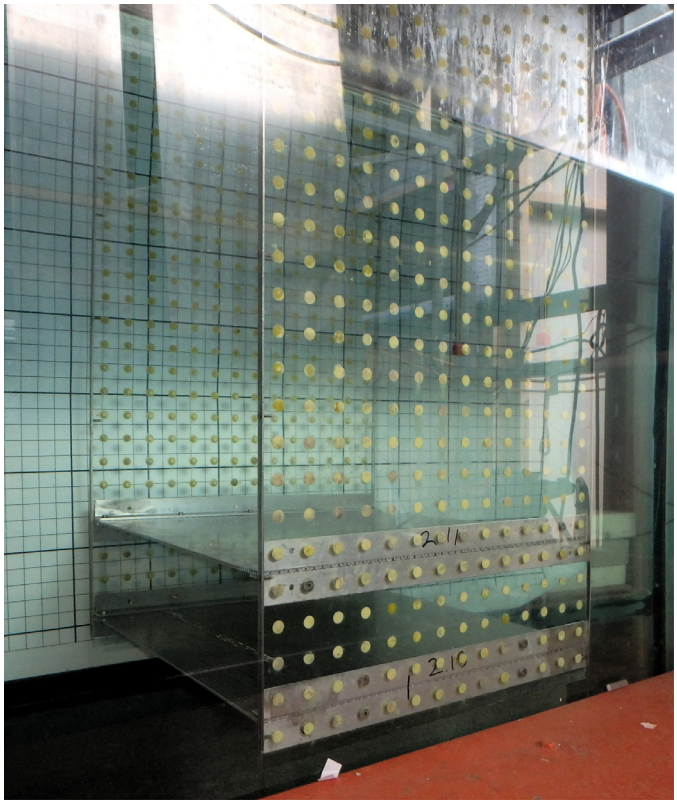

Fig. 1. Photo of the present experimental test setup. Parallel perforated plates (2P28_120) placed inside the acrylic glass plates of the experimental rig.

used to fasten the structure to the acrylic glass plates, give a small added mass contribution for KC → 0. The stiffeners and fastening profiles fitted to the plates are accounted for when calculating the perforation ratio.

We measure the vertical motions, vertical force and wave elevations during the forced oscillation tests. The test series include five oscillation periods, T = 1.00 s, 1.25 s, 1.50 s, 1.75 s and 2.00 s, and a range of amplitudes from 1.7 cm to 13 cm, corresponding to 0.25 ≤ KC ≤ 2. The experimental results are presented with different markers for the five forcing periods, diamonds (T = 1.00 s), pentagons (1.25 s), hexagons (1.50 s), circles (1.75 s), and stars (2.00 s). Several accelerometers are used to monitor both the (wanted) vertical and (possible) horizontal motions of the configurations. Measurements of the vertical force, motions and wave elevations are sampled at 200 Hz with Butterworth filtering at 20 Hz. The measurements are band-pass filtered around the basic harmonic of the oscillation when calculating the wave elevations, hydrodynamic coefficients and normalized hydrodynamic force amplitude. The applied instrumental setup was carefully set up to achieve zero phase delay between the different signals, in order to obtain reliable hydrodynamic force coefficients.

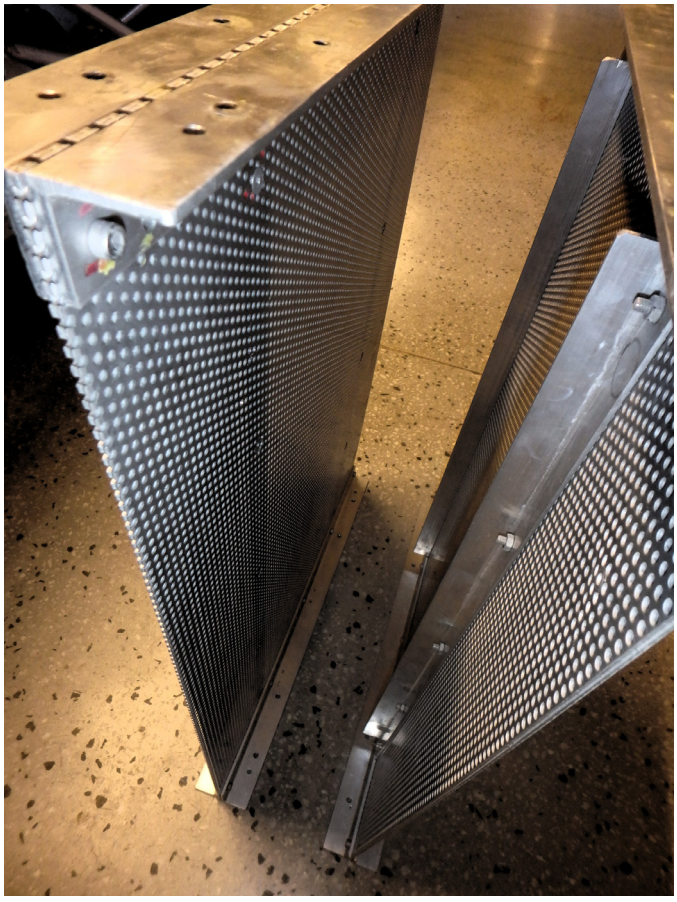

Fig. 3. Photo of the two perforated plates of 2P28. Each plate consists of approximately 10,000 circular holes. The perforated plates have profiles along the length span to increase stiffness.

The present experimental setup yields conditions that are close to an infinite fluid domain. Nevertheless, since the water depth is limited to h = 1.0 m, some influence from the boundaries should be expected. The increase in added mass coefficient for a circular cylinder close to the free-surface or a wall is discussed by Faltinsen [17, p. 54]. When the distance to the boundary is larger than the diameter of the cylinder, the increase in the added mass of the cylinder is rather small, around 10% and decreasing for increasing distance [17, Fig. 3.11]. In the present experimental investigations, the distance to the boundaries for the largest configuration (44 cm) is slightly larger than the width of the plates (42 cm). Further, the added mass of the perforated plates is very small at small KC numbers since the numerous openings allow water to flow without circumventing the plate. However, for larger KC numbers, the added mass increases rapidly due to blocking of flow through the perforated openings. Moreover, the oscillating plates will generate

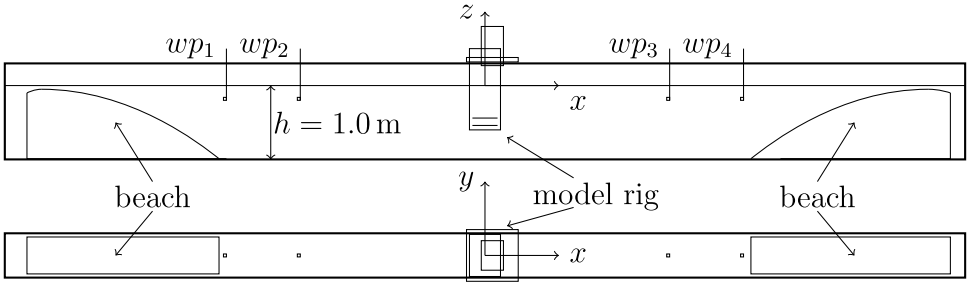

Fig. 2. Sketch of the tank setup during experimental investigations. Upper: Side view. Lower: Bird's eye view. The tank is approximately 13.5 m long and 0.60 m wide. The water depth is h = 1.0 m. The position of the model rig, wave probes and beaches are indicated.

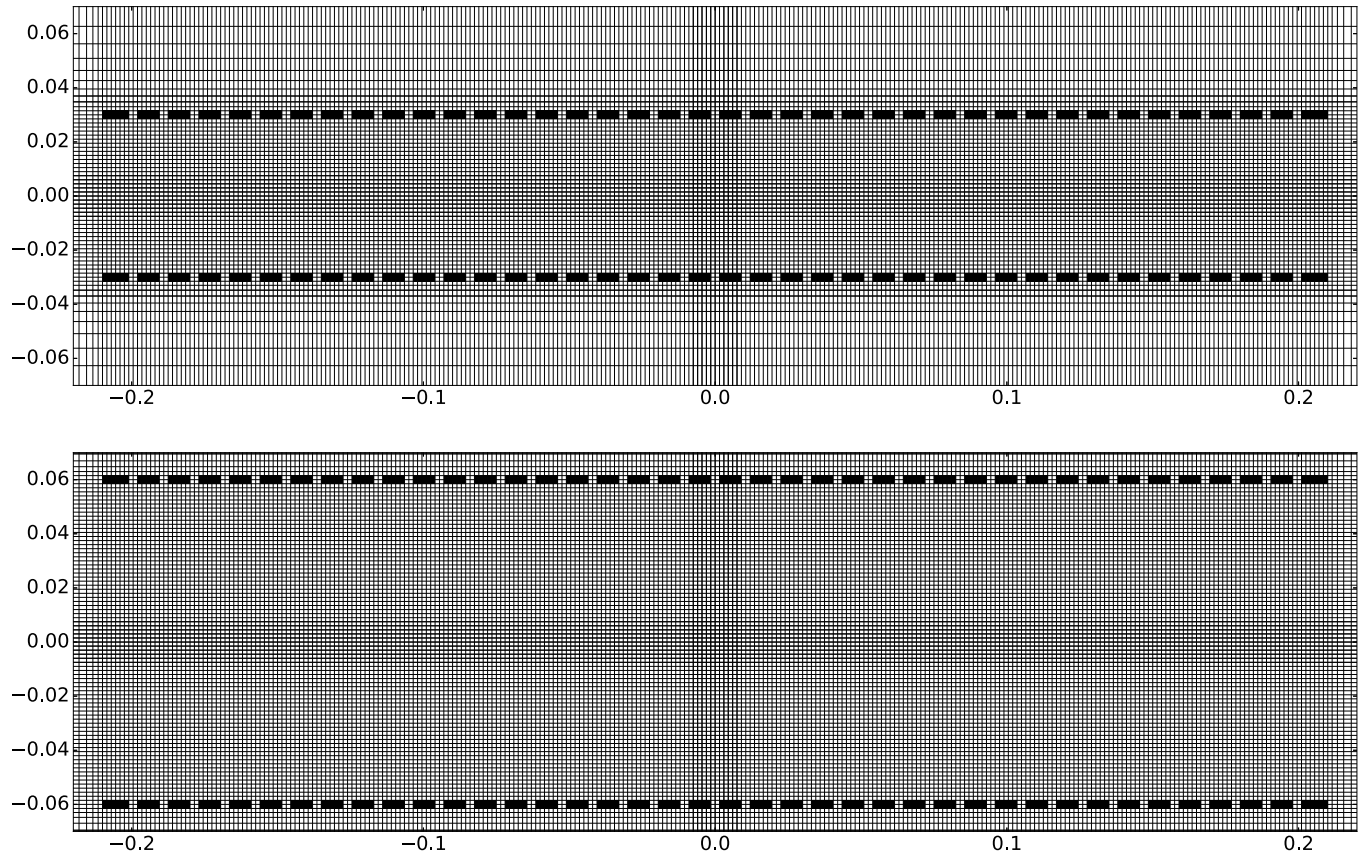

Fig. 4. Illustration of the fine region of the discretization of the 2P28_60 (top) and 2P28_120 (bottom) numerical models. The total domain size is 6 m × 6 m and the total number of grid cells are 80216 (2P28_60) and 96252 (2P28_120). A section of the 2P28_60 grid is presented in Fig. 5 for easier visualization of the mesh density.

waves that have some influence on the hydrodynamic coefficients. The radiated waves are measured by wave probes downstream of the rig. A plot of the corresponding wave-radiation damping coefficients [17, p. 47], is included in the result section. In general, the wave-radiation damping coefficients are small for the tested forcing amplitudes and periods of oscillations. We conclude from this that the setup yields conditions that are close to an infinite fluid domain.

4. Numerical simulations

Numerical results (CFD) are obtained from a two-dimensional Navier–Stokes solver, developed earlier in our study [3]. The CFD uses a staggered grid approach. The governing equations are solved on rectilinear grids with a fine resolution region close to the discretized perforated plates, and gradually larger cells away from the structure.

Table 1
Characteristics of the presently experimentally tested perforated plates. D is the width of the plates, t the thickness of each plate. M is the dry weight of each plate. The distance between the parallel plates is 60 mm (2P28_60) and 120 mm (2P28_120).

Perforation	Openings	D	t	M
$\tau = 0.28$	$\approx$ 10,000 circular holes	420 mm	3 mm	2.12 kg

We follow previous findings using the CFD for simulation of perforated plates, regarding grid size and stretching, the size of the numerical domains and the number of fluid cells between each plate element [3].

The present CFD solves the governing equations of isothermal flows of a homogeneous Newtonian fluid with negligible bulk viscosity, the

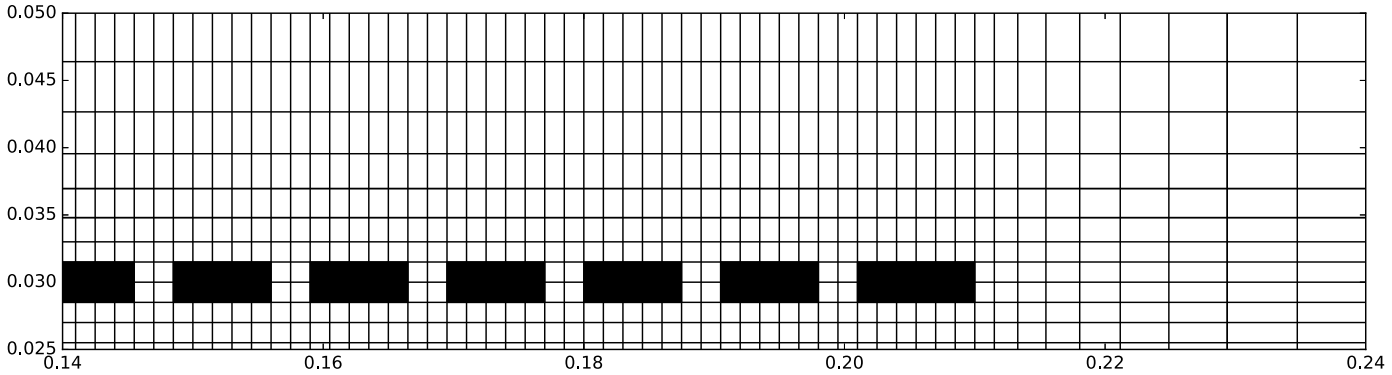

Fig. 5. Upper-right part of the fine region of the discretization of the 2P28_60 grid, cf. Fig 4. Similar stretching and equal discretization of the plates is used for 2P28_120.

continuity and momentum equations, by use of a fractional-step method, as that by Chorin [18], where the momentum equation is split into two steps,

$$\frac{u_i^* - u_i^n}{\Delta t} = -u_j \frac{\partial u_i}{\partial x_j} + \nu \frac{\partial^2 u_i}{\partial x_j^2}, \tag{8}$$

$$\frac{u_i^{n+1} - u_i^*}{\Delta t} = -\frac{1}{\rho}\frac{\partial p}{\partial x_i}. \tag{9}$$

Standard index notation is used; u_i represents the velocity component in the x_i direction. For simplicity, the velocity components are referred to as $u = u_1$ (horizontal direction) and $w = u_2$ (vertical direction). The fluid density, ρ, and kinematic viscosity, ν, are set to values similar to the water properties of the experimental investigations, $\rho = 1000\ \mathrm{kgm^{-3}}$ and $\nu = 1 \times 10^{-6}\mathrm{m^2 s^{-1}}$. n represents the present time-step, $n+1$ the next time-step, and * an auxiliary step. Since the velocity field at $n+1$ is divergence free, the divergence of Eq. (9) yields a Poisson equation for the pressure, p,

$$\frac{\partial^2 p}{\partial x_i^2} = \frac{\rho}{\Delta t}\frac{\partial u_i^*}{\partial x_i}. \tag{10}$$

For each time-step, Eq. (8) is solved to find the tentative velocity field. Then Eq. (10) is used to determine the pressure, before the velocity field at $n+1$ is found from Eq. (9). The three steps of the procedure are as follows:

1. u^n, $w^n \rightarrow u^*$, w^*
2. u^*, $w^* \rightarrow p^{n+1}$
3. u^*, w^*, $p^{n+1} \rightarrow u^{n+1}$, w^{n+1}.

Spatial discretizations in the CFD are of first and second orders. The diffusion terms of Eq. (8), the pressure gradient terms of Eq. (9), as well as the terms of Eq. (10), are solved with second-order accurate central difference schemes unless else is explicitly highlighted. The spatial discretization of the advection terms is performed using the first order upwind scheme. The advection terms are linearized in time using the previous known velocity, i.e. u_j^n of Eq. (8).

Time-stepping is performed using the implicit Euler scheme. The time-step size is chosen based on requirements to ensure at least 200 time-steps per period of oscillation, and a CFL number smaller than one in all cells,

$$\Delta t = \min\left(\frac{T}{200}, \frac{\Delta x}{u}, \frac{\Delta z}{w}\right). \tag{11}$$

The simulations of the two parallel configurations, 2P28_60 and 2P28_120, are performed using similar grids. We model each of the perforated plates with 40 plate elements per plate. Each plate is 3 mm thick, as in the experiments. Two grid cells are used in each opening between the plate elements. This perhaps surprisingly (locally) coarse grid was found sufficient in the mesh refinement study of [3]. A fine region of grid cells is used in the proximity of the two parallel plates. The fine region is larger for 2P28_120 than for 2P28_60, due to the larger gap between the two parallel plates, with larger number of grid cells and higher computational costs as consequence. Stretched grid cells, with increasingly larger cells away from the structure, are used towards the boundaries of the computation domain. Illustrations of the fine regions of the two configurations are presented in Figs. 4 and 5.

4.1. Oscillating flow conditions

The boundary conditions in oscillating flow are illustrated in Fig. 6. In oscillating flow conditions, the velocity field at the borders of the computational domain is set to a prescribed oscillating vertical velocity based on the given KC number,

$$u = 0, \tag{12}$$

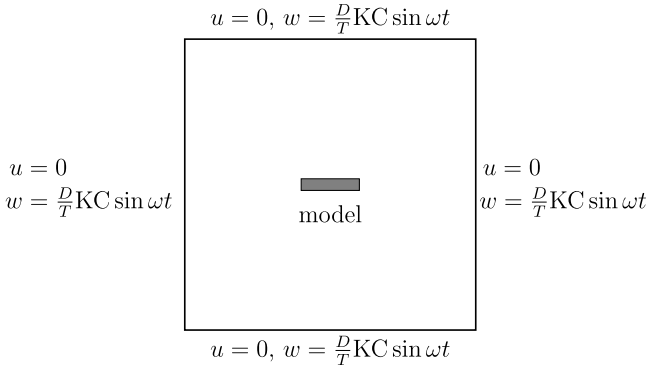

Fig. 6. Oscillating flow setup. The ambient vertical velocity component is oscillating harmonically on the boundaries. The simulated model is placed in the center of the numerical domain.

$$w = \frac{D}{T}\mathrm{KC}\sin\omega t. \tag{13}$$

The period of oscillation (and corresponding circular frequency $\omega = \frac{2\pi}{T}$) is set to $T = 1.0$ s to yield similar Reynolds numbers as in the experiments, although the Reynolds number is expected not to be of importance since the perforated plates have sharp-edged openings. Hence $\frac{D}{T}$ is a constant ($0.42\ \mathrm{ms^{-1}}$) in all oscillating flow simulations.

Appropriate boundary conditions for the pressure gradient are obtained from the Navier–Stokes equation,

$$\frac{\partial p}{\partial x} = -\rho\frac{\partial u}{\partial t} = 0, \tag{14}$$

$$\frac{\partial p}{\partial z} = -\rho\frac{\partial w}{\partial t} = -\rho\omega\frac{D}{T}\mathrm{KC}\cos\omega t. \tag{15}$$

No-slip conditions are used on the boundaries of the discretized structure elements,

$$u = w = 0, \quad \frac{\partial p}{\partial x} = \frac{\partial p}{\partial z} = 0. \tag{16}$$

4.2. Orbital flow conditions

The boundary conditions in orbital flow are illustrated in Fig. 7. Except for non-zero horizontal prescribed velocities and accelerations, the orbital flow simulations are performed in the exact same manner as the oscillating flow simulations. The following velocity conditions are set on the boundaries of the computational domains,

$$u = -\frac{D}{T}\mathrm{KC}\cos\omega t, \tag{17}$$

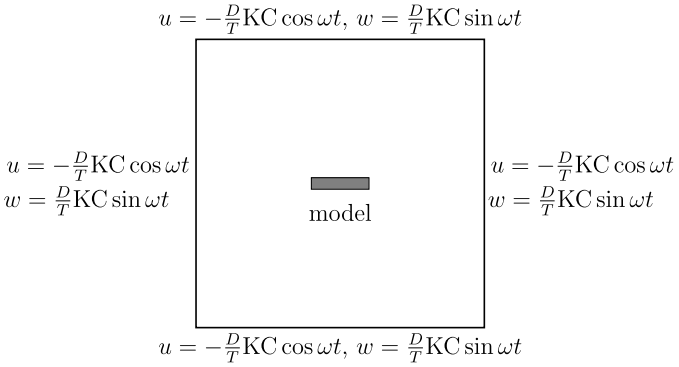

Fig. 7. Orbital flow setup. The ambient horizontal and vertical velocity components are oscillating harmonically on the boundaries. The simulated model is placed in the center of the numerical domain.

$$w = \frac{D}{T}\mathrm{KC}\sin\omega t, \tag{18}$$

with corresponding appropriate boundary conditions for the pressure gradient based on the prescribed accelerations.

Orbital flow conditions may be regarded as a limit of linear wave theory, where the wave is long compared to the model and the model is deeply submerged, such that there is no interaction with a free surface. A benefit of this approach is that simulations can be set up similar to oscillating flow conditions.

4.3. Potential flow added mass calculation

Added mass coefficients in the limit of zero KC are computed with a source method (BEM). The potential flow solver has been verified and checked for convergence for a single circular cross-section and a single square cross-section [1].

Two sets of BEM calculations are performed: 1) BEM for experimental models and 2) BEM for CFD models. The perforated plates used in the experiments are close to ideal—they are relatively flat ($\frac{D}{t} = 140$) and consist of numerous holes ($N \approx 10000$). The added mass coefficient in the limit of zero KC of an ideal perforated plate is zero [6]. Therefore, the expected added mass for KC → 0 is due to the stiffeners and fastening profiles, cf. Fig. 3. An estimation of the added mass due to these is calculated with the BEM. The second set of BEM results are calculated by using the discretized CFD models of 2P28_60 and 2P28_120, cf. Fig. 4. The CFD models of 2P28_60 and 2P28_120 consist of 80 small rectangular boxes. For computational reasons, we use 32 sources per box when calculating the potential flow added mass, that is, 2560 sources in total.

5. Results

5.1. Added mass calculations with BEM

Potential flow results for 2P28_60 and 2P28_120 are presented in Table 2. The BEM models of the experimentally investigated 2P28_60 and 2P28_120 are based on the assumption that the contribution from the perforated plates are zero, and only due to the stiffeners and fastening profiles on the two plates into account. Contrary, the CFD models of 2P28_60 and 2P28_120, which consist of 80 small rectangular cross sections with openings between them, are, in the BEM, modeled exactly as in the corresponding CFD models. The zero KC-limit added mass is small, and within 8% of that of a solid flat plate; A_0 is the zero KC-limit added mass of a single solid flat plate.

5.2. 60 mm gap

Results from the experimental investigations and numerical simulations are presented in the following. The different markers of the experiments indicate the five tested forcing periods, T = 1.00 s (diamonds), 1.25 s (pentagons), 1.50 s (hexagons), 1.75 s (circles) and 2.00 s (stars). We use the same markers to indicate the periods of oscillations from the forced oscillation experiments in all figures. The markers are presented with and without error bars in Fig. 8.

Table 2
Potential flow solver added mass results (BEM) and Froude–Krylov contributions for the parallel perforated plates configurations. A_0 is the analytical added mass of a solid plate. V is the volume of the structure.

	2P28_60 exp.	2P28_120 exp.	2P28_60 CFD	2P28_120 CFD
$\frac{A}{A_0}$	0.0371	0.0385	0.0647	0.0652
$\frac{\rho V}{A_0}$	0.0131	0.0131	0.0131	0.0131
$\frac{A+\rho V}{A_0}$	0.0502	0.0517	0.0779	0.0784

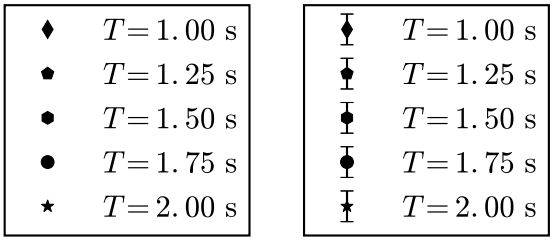

Fig. 8. Markers used to present results of different periods of oscillation from forced oscillation experiments.

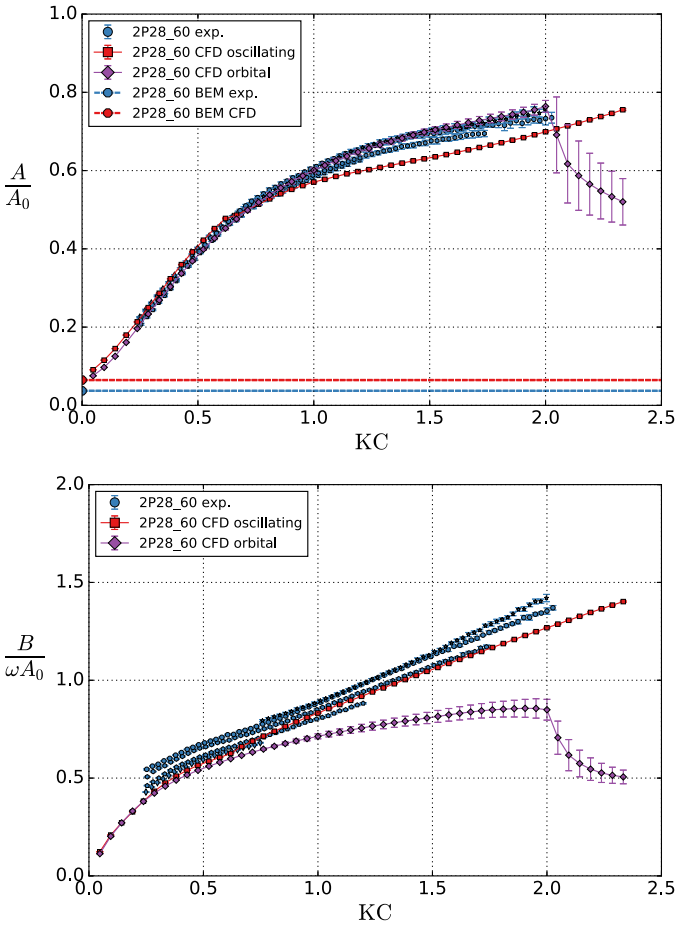

Fig. 9. Added mass and damping coefficients from forced oscillation experiments of parallel plate configuration 2P28_60 (five different periods of oscillation). Numerical results in terms of potential flow (BEM), and CFD results using oscillating and orbital flow conditions.

The added mass and damping coefficients from experimental and numerical investigations of 2P28_60 are presented in Fig. 9. The coefficients increase with increasing KC number. There is in general little period dependence in added mass experimental investigations, but some for the damping. The hydrodynamic coefficients are, in general, well predicted by the CFD. It appears that the numerical model, which has previously been used for single plates, captures the dominant effects also for parallel plates. The limiting added mass values for small KC predicted by the CFD is consistent with the numerical results for KC → 0 predicted by the BEM.

Two different potential flow added mass coefficients are presented for KC = 0, one for the experimental structure (BEM exp.) and one for the CFD models (BEM CFD). Both seem reasonable compared with the experimental results and numerical simulations.

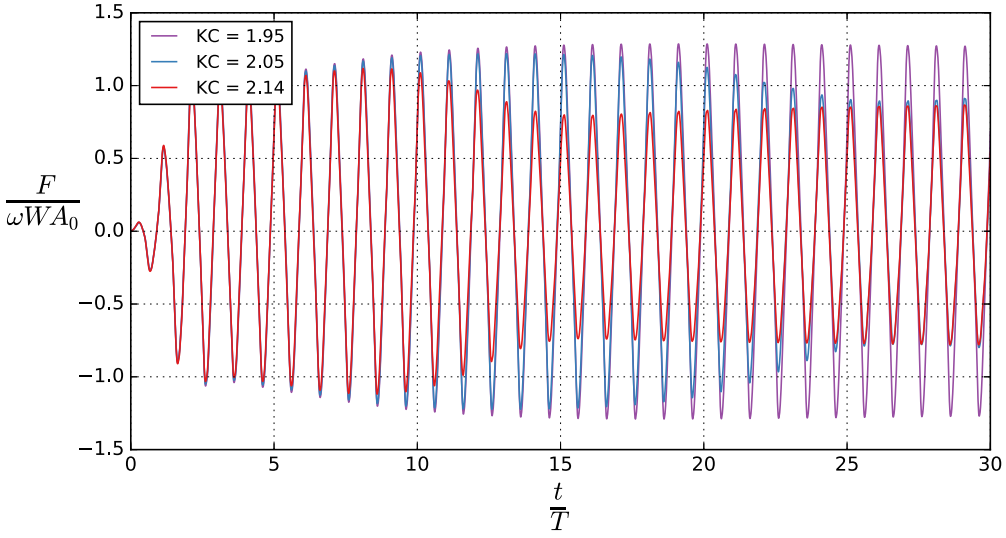

Fig. 10. Normalized force on 2P28_60 in orbital flow conditions at KC = 1.95, 2.05 and 2.14 for the simulated 30 periods of oscillation.

The orbital flow conditions yields similar added mass coefficients as in oscillating flow for KC $\leq$ 2. For larger KC numbers, the added mass coefficient abruptly decreases. Notably, the standard deviations become larger, indicating larger differences in the added mass coefficients from cycle to cycle. A shift in behavior at KC = 2 is found for the damping coefficient as well. The orbital flow deviates more from the oscillating flow for the damping coefficient than for the added mass coefficient, yielding smaller coefficients than corresponding oscillating flow simulations for all KC $>$ 0.3.

In Fig. 10, the force on 2P28_60 in orbital flow conditions at KC = 1.95, 2.05 and 2.14, for the whole length of the simulation, is presented. For KC = 1.95, the force increases from the ramp and reaches what seems to be near steady-state after the first 10–12 periods of oscillation. Contrary, for KC = 2.05 and KC = 2.14 the force decreases after an initial increase, and then oscillates with a smaller amplitude of motion during the rest of the simulation. These variations in force amplitude yield large standard deviations in the coefficient plots since we use a time-window extending from $t = 5T$ to the end of the simulation, $t = 30T$.

5.3. 120 mm gap

The added mass and damping coefficients from experimental and numerical investigations of 2P28_120 are presented in Fig. 11. As for 60 mm gap, the agreement between the experimental and numerical oscillating flow results is notable, particularly for the added mass coefficients. The limiting value of added mass as KC $\rightarrow$ 0 is consistent between experiments, CFD and BEM.

Contrary to the forced oscillation tests, where both coefficients increase for increasing KC number, the coefficients from orbital flow simulations reach a maximum at KC $\approx$ 1.5. For KC $>$ 1.5, a drop in coefficients for increasing KC numbers, similar to that found for 2P28_60 at KC $>$ 2.0, is found. The orbital flow results deviates from the oscillating flow results, in general, more for the damping coefficients than for the added mass coefficients. The large standard deviations in orbital flow coefficients for KC $>$ 1.5 are due to variations in force amplitude obtained from the simulation, similar to the variations found for 2P28_60, cf. Fig. 10.

There is little period dependency in the experimental results, but somewhat more than what was found for 2P28_60. A possible reason is that the configuration is larger and the top plate is closer to the free surface.

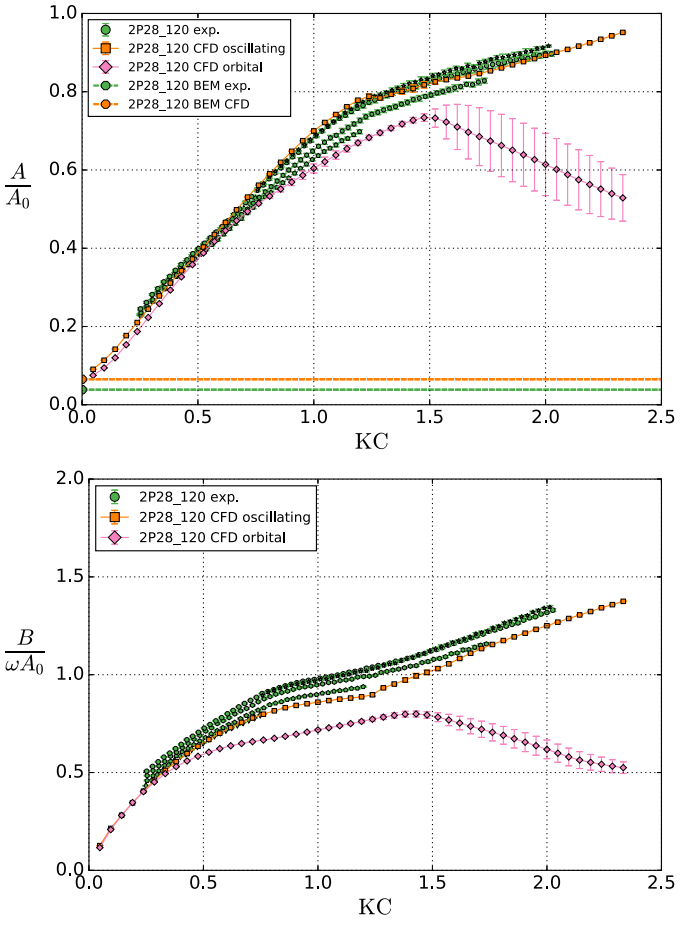

Fig. 11. Added mass coefficients from forced oscillation experiments of parallel plate configuration 2P28_120 (five different periods of oscillation). Numerical results in terms of potential flow (BEM), and CFD results using oscillating and orbital flow conditions.

5.4. Wave-radiation damping

Dimensionless damping coefficients due to radiated waves, $\frac{B_w}{\omega A_0}$, during the forced oscillation experiments of both 2P28_60 and 2P28_120, are plotted in Fig. 12. The wave-radiation damping coefficients increase, in general, with increasing KC number, and depend on

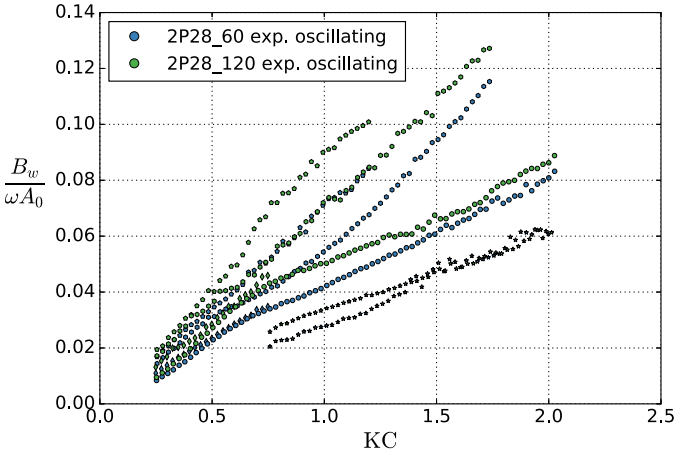

Fig. 12. Wave-radiation damping, B_w, due to radiated waves in the forced oscillation experiments of P28_60 and P28_120. The different markers indicate the five tested periods of oscillation, $T = 1.0$ s (diamonds), 1.25 s (pentagons), 1.5 s (hexagons), 1.75 s (circles) and 2.0 s (stars).

the period of oscillation. The largest configuration (2P28_120) yields, in general, somewhat larger wave-radiation damping coefficients than the smallest configuration (2P28_60).

Typically, the wave-radiation damping coefficients are 4–8% of the total damping, cf. Fig. 9. For oscillation periods $T = 1.25$ s and $T = 1.5$ s, the largest tested KC numbers yield wave-radiation damping that exceed 8% of the total damping. The largest relative wave-radiation damping is obtained for 2P28_120 with oscillation period $T = 1.5$ s, where, for KC = 1.7, the wave-radiation damping is 11% of the total damping.

We note that the slight underestimation of the damping coefficients predicted with CFD (which is infinite fluid domain), cf. Fig. 9, is of same order as the wave-radiation damping contributions in the experiments.

5.5. Normalized force amplitude

The normalized force amplitude, i.e. the square root of the sum of the normalized added mass and damping coefficients squared, Eq. (7), for 2P28_60 and 2P28_120 is presented in Fig. 13. This presentation clearly illustrates a reduction in force in orbital flow conditions.

There are relatively small differences in the normalized force

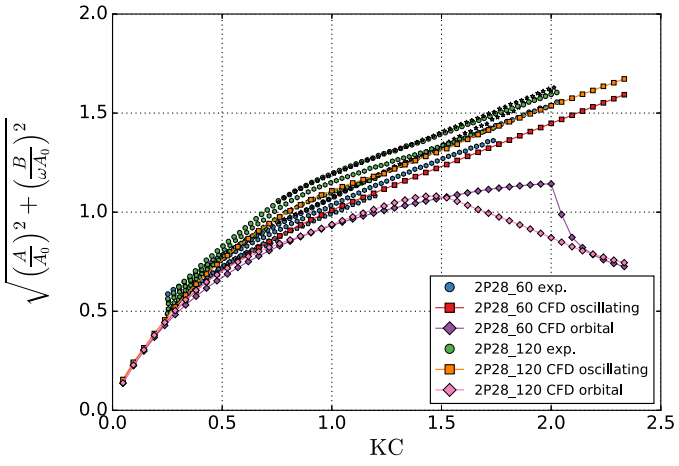

Fig. 13. Normalized force amplitude, i.e. the square root of the sum of the normalized added mass and damping coefficients squared, from forced oscillation experiments of 2P28_60 and 2P28_120 (five different periods of oscillation), and CFD results from numerical simulations of oscillating flow conditions and orbital flow conditions.

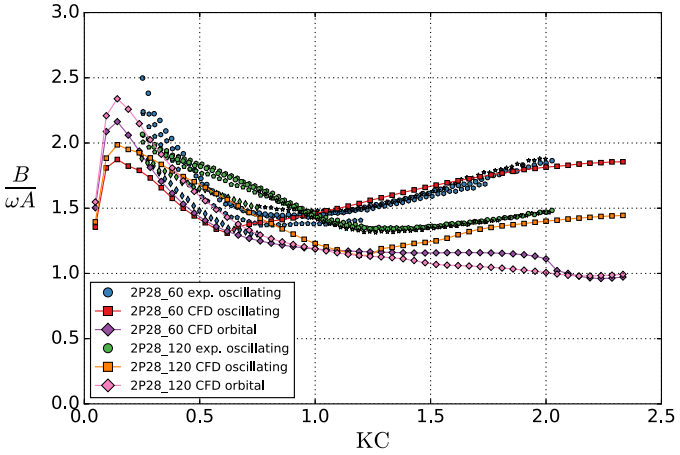

Fig. 14. Damping to added mass force ratio from forced oscillation experiments of P28_60 and P28_120 (five different periods of oscillation). Numerical results (CFD) for oscillating and orbital flow conditions.

amplitude between the two configurations. The gap distances relative to the width of the plates are 0.14 (2P28_60) and 0.29 (2P28_120). The force is in general somewhat larger for the configuration with the largest gap, but the dependence of the KC number is much more important than the dependence on the gap distance.

5.6. Damping-to-added mass ratio

The ratio of the damping force to the added mass force of both 2P28_60 and 2P28_120 is presented in Fig. 14. Both parallel plate configurations are damping dominant in oscillating flow for all tested KC numbers, that is, $\frac{B}{\omega A} > 1$.

The effect of gap distance is rather modest in the investigated range. The experimental results yield, in general, decreasing damping dominance for increasing gap distance. An exception is for $0.5 < KC < 0.9$ where the damping dominance is larger for 2P28_120 than for 2P28_60. For $KC > 0.9$, the configuration with the smaller gap yields the largest damping dominance.

There are some differences in damping dominance between orbital and oscillating flow conditions for the two parallel configurations. In oscillating flow, there is damping dominance in the whole KC number range. In orbital flow conditions, for the very largest simulated KC numbers, orbital CFD predicts an approximately equal importance of the damping force and the added mass force.

5.7. Force differences on upper and lower plates

Interaction effects between the upper and the lower plates affect the forces on the structures. When the prescribed vertical velocity is positive, the upper perforated plate will be in the wake of the lower plate, and vice versa. Consequently, the difference in forces on the upper and lower perforated plate should be expected to depend on the distance between the upper and the lower plates, and on the KC number.

In Figs. 15–18, we present time series of the forces on the upper and lower plates of 2P28_60 and 2P28_120 during an oscillation cycle in oscillating flow conditions. The flow is fully developed at the time of the considered oscillation period, $m = 21$ ($20T < t \leq 21T$). Two different KC numbers are considered, KC = 0.2 and KC = 1.0. We have included results for one single perforated plate, denoted P28. The P28 plate is modeled identically as the two perforated plates of 2P28.

The forces on 2P28_60 are presented in Figs. 15and 16. For the smaller KC number, KC = 0.2, there is almost no difference in the forces on the upper and the lower plates. Compared to the corresponding single plate, there is a small phase difference and a reduction in force magnitude. The peak in force is shifted to the left, meaning an increase,

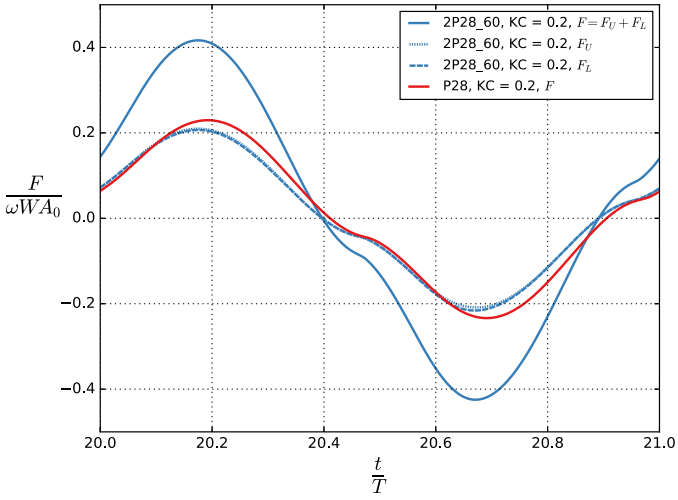

Fig. 15. Normalized force on 2P28_60 during an oscillation cycle at KC = 0.2. The force on the upper plate and the lower plate are presented, in addition to the sum of the force on both plates. Comparisons with a corresponding single plate.

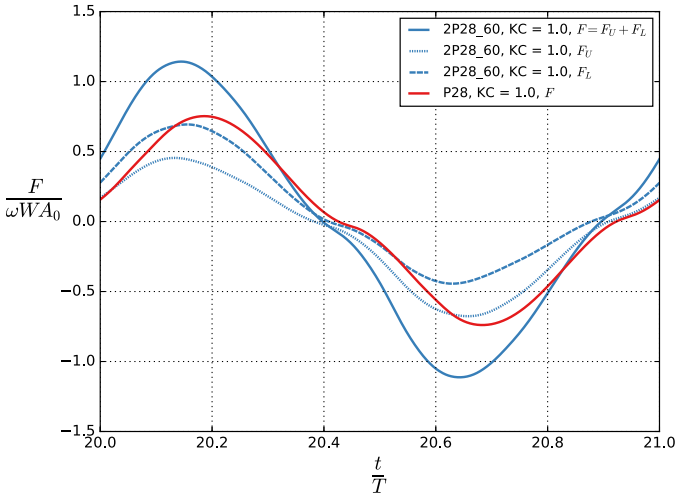

Fig. 16. Normalized force on 2P28_60 during an oscillation cycle at KC = 1.0. The force on the upper plate and the lower plate are presented, in addition to the sum of the force on both plates. Comparisons with a corresponding single plate.

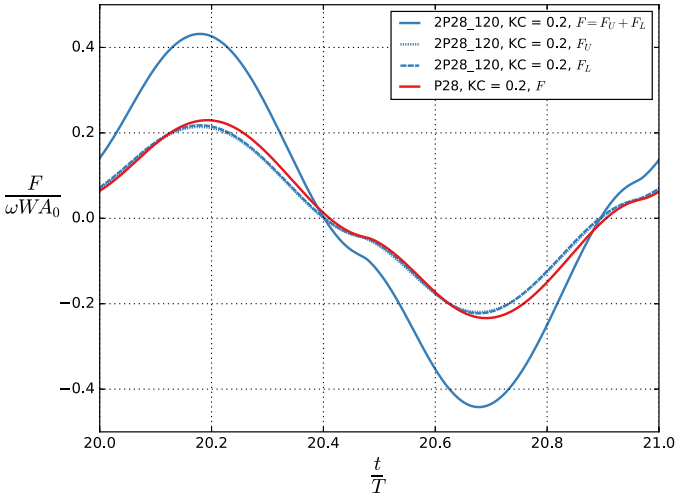

Fig. 17. Normalized force on 2P28_120 during an oscillation cycle at KC = 0.2. The force on the upper plate and the lower plate are presented, in addition to the sum of the force on both plates. Comparisons with a corresponding single plate.

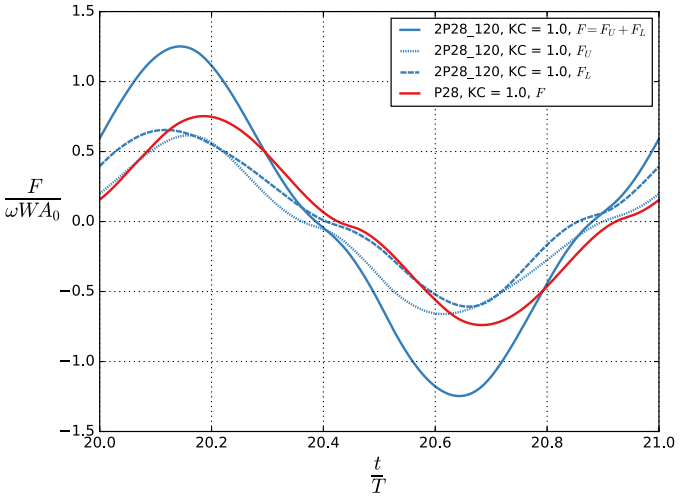

Fig. 18. Normalized force on 2P28_120 during an oscillation cycle at KC = 1.0. The force on the upper plate and the lower plate are presented, in addition to the sum of the force on both plates. Comparisons with a corresponding single plate.

compared to the single plate, in added mass relative to damping. For the larger KC number, KC = 1.0, substantial differences are found. We observe a considerable phase difference compared to the single plate. The force magnitude on both plates of the parallel configuration are smaller than the corresponding single plate, in particular for the plate that is downstream, that is, the upper plate during the first half cycle and the lower plate during the second half cycle.

We would like to emphasize that since the nondimensional force amplitude is increased by a factor of four from KC = 0.2 to KC = 1.0 (cf. the vertical axis in the figure), the actual force amplitude is increased by a factor twenty. This has important practical consequences, and exemplifies the nature of perforated plates in water.

Corresponding plots for 2P28_120 are presented in Figs. 17 and 18. For the smallest KC number, we observe similar results as for 2P28_60. Close inspection, however, reveals that increasing the gap between the two plates has an effect even at KC = 0.2; the forces on the upper and the lower plates are more similar to that of a single plate than for 2P28_60. For the larger KC number, the magnitude of the force on the downstream plate is less reduced compared to 2P28_60. This is expected since the two plates are placed further away from each other in 2P28_120. However, there are larger differences in the phases of the forces with 2P28_120, compared to that of the single plate, than for the 2P28_60 configuration.

5.8. On the force reduction in orbital flow conditions

The force reduction in orbital compared to oscillating flow conditions is found to depend on the gap between the two perforated plates in parallel. For 2P28_60, the maximum normalized force amplitude in orbital flow occurs for KC = 2.00, whereas the corresponding maximum is at KC = 1.43 for 2P28_120. To investigate the effect on the total force of the configuration, caused by interaction between the two plates in orbital motion, we study flow visualization plots of 2P28_60 at KC = 1.95 and KC = 2.05, that is, slightly below and above KC = 2.0 which yields the largest normalized force amplitude.

In Figs. 19–21, streamline plots of 2P28_60 in orbital flow conditions for KC = 1.95 and KC = 2.05 are presented. The plots are obtained at three different time-steps early in the oscillation cycle. The arrow

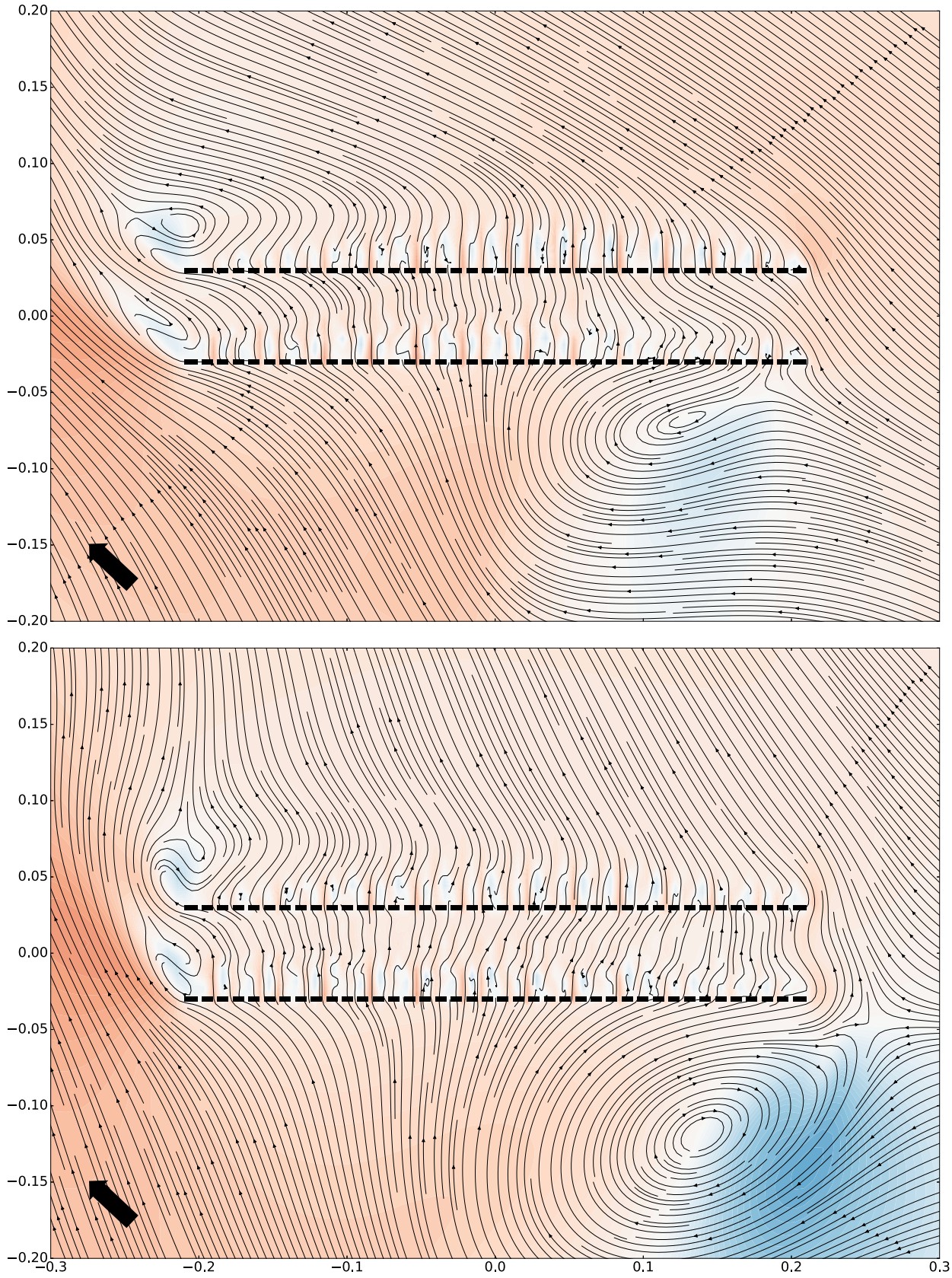

Fig. 19. Flow visualizations of 2P28_60 with orbital flow conditions for KC = 1.95 (top) and KC = 2.05 (bottom). The time-instant is $0.12T$ into an oscillation period ($u = -\frac{D}{T}\mathrm{KC}\cos\omega t$, $w = \frac{D}{T}\mathrm{KC}\sin\omega t$). The color map for the contours represent the vertical velocity (red for positive, blue for negative). (For interpretation of the references to color in this figure legend, the reader is referred to the web version of this article.)

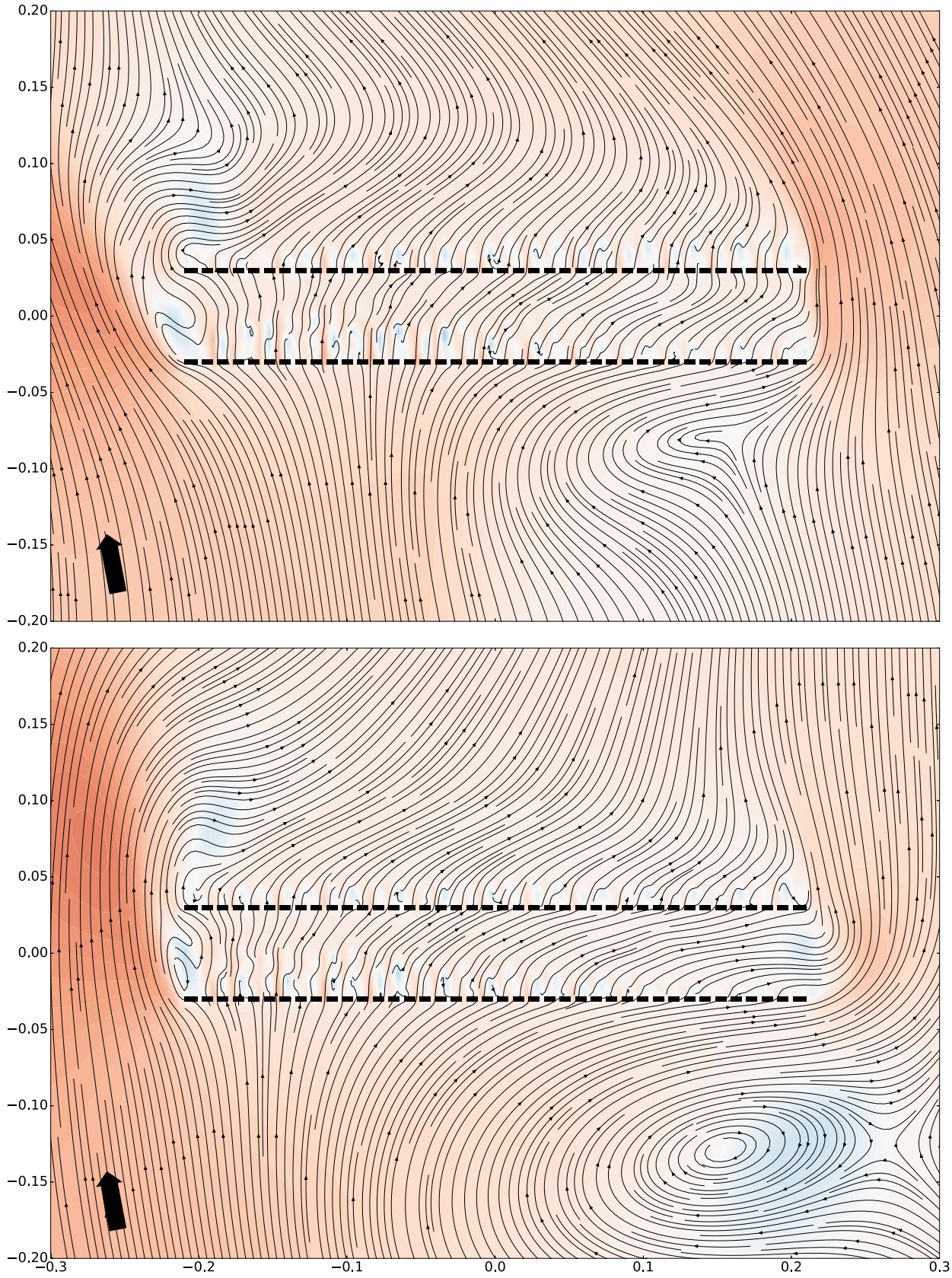

Fig. 20. Flow visualizations of 2P28_60 with orbital flow conditions for KC = 1.95 (top) and KC = 2.05 (bottom). The time-instant is $0.22T$ into an oscillation period ($u = -\frac{D}{T}\mathrm{KC}\cos\omega t$, $w = \frac{D}{T}\mathrm{KC}\sin\omega t$). The color map for the contours represent the vertical velocity (red for positive, blue for negative). (For interpretation of the references to color in this figure legend, the reader is referred to the web version of this article.)

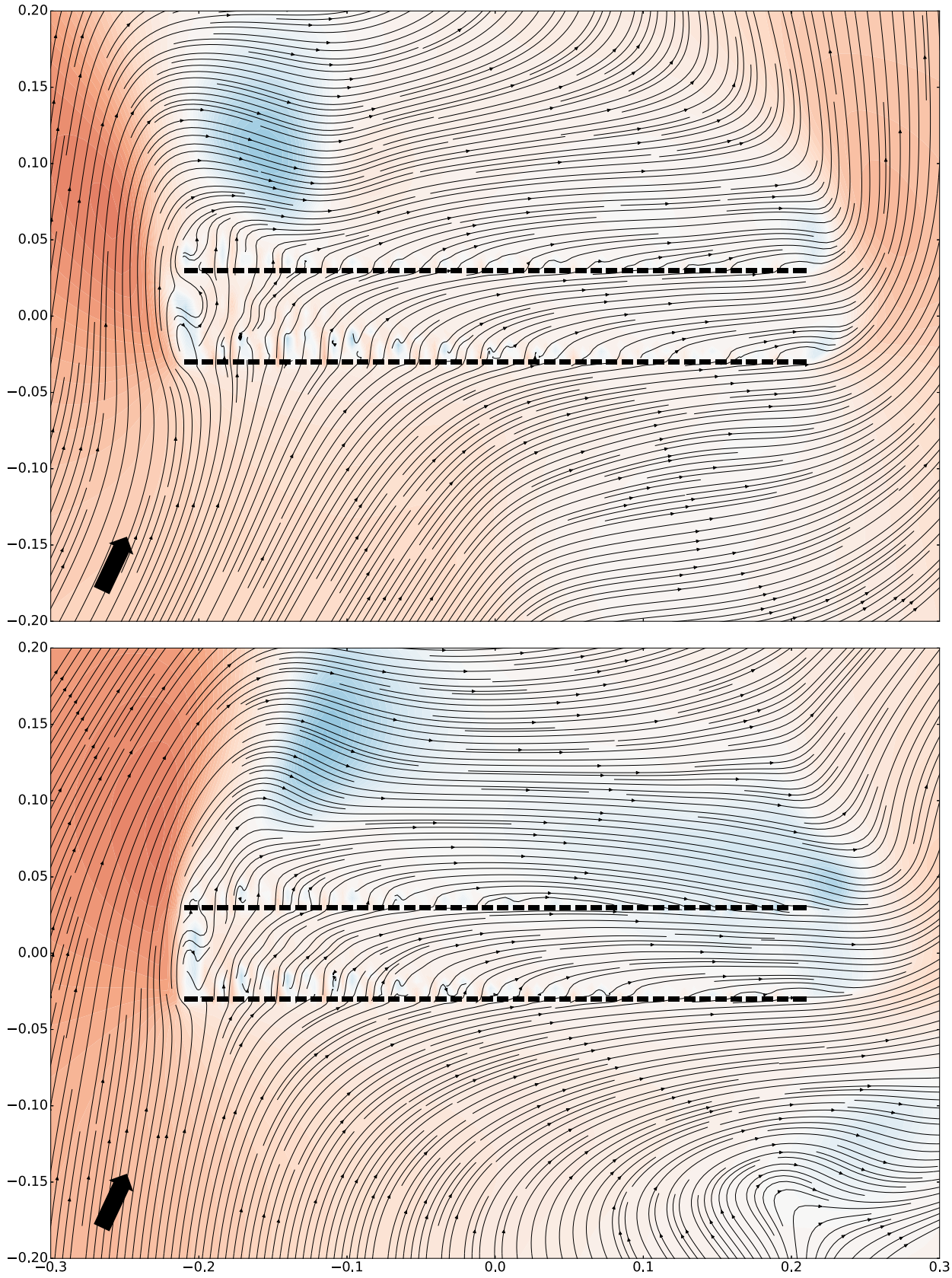

Fig. 21. Flow visualizations of 2P28_60 with orbital flow conditions for KC = 1.95 (top) and KC = 2.05 (bottom). The time-instant is $0.32T$ into an oscillation period ($u = -\frac{D}{T}\mathrm{KC}\cos\omega t$, $w = \frac{D}{T}\mathrm{KC}\sin\omega t$). The color map for the contours represent the vertical velocity (red for positive, blue for negative). (For interpretation of the references to color in this figure legend, the reader is referred to the web version of this article.)

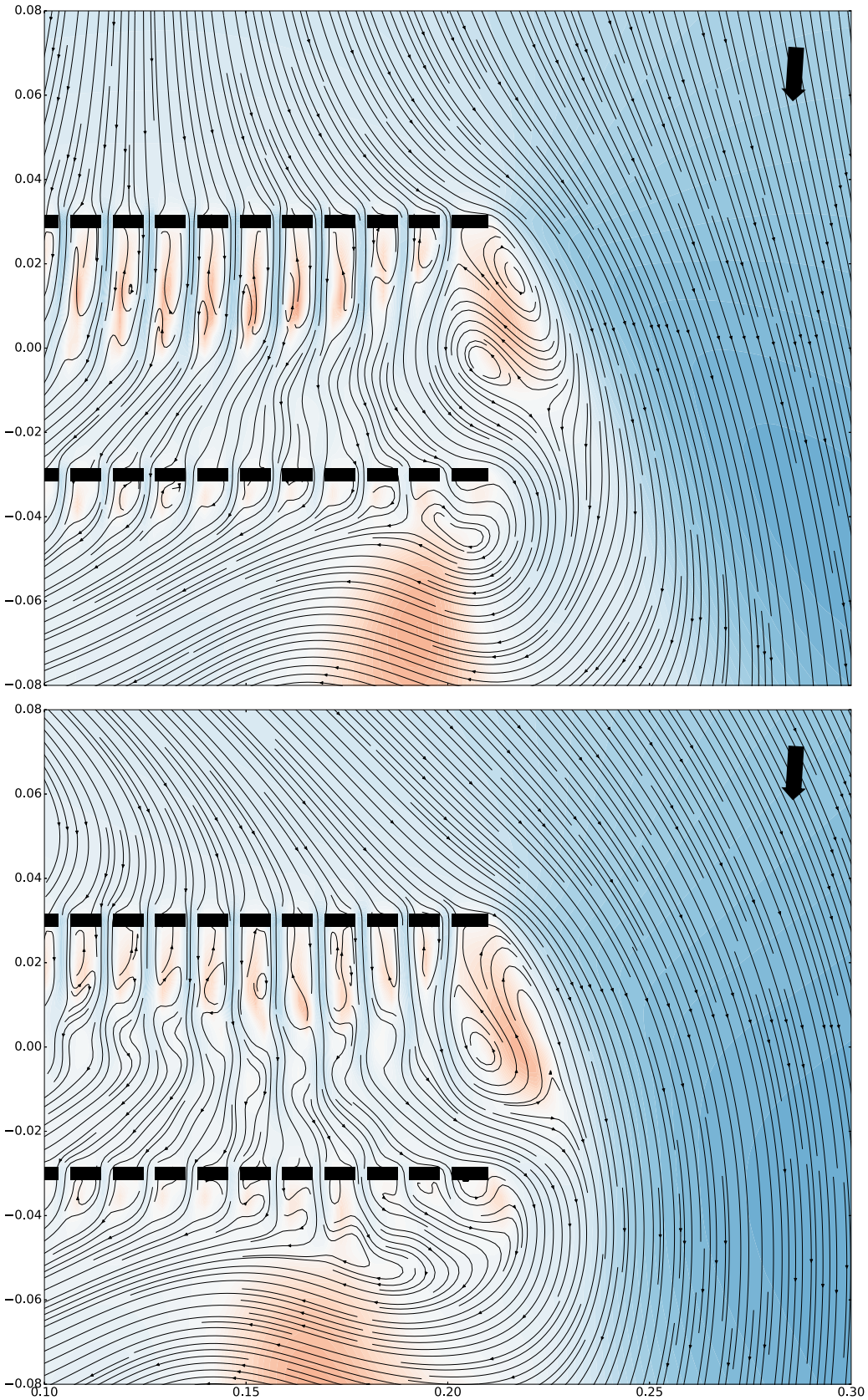

Fig. 22. Flow visualizations zoomed in on the right part of 2P28_60 with orbital flow conditions for KC = 1.95 (top) and KC = 2.05 (bottom). The time-instant is $0.76T$ into an oscillation period ($u = -\frac{D}{T}\mathrm{KC}\cos\omega t$, $w = \frac{D}{T}\mathrm{KC}\sin\omega t$). The color map for the contours represent the vertical velocity (red for positive, blue for negative). (For interpretation of the references to color in this figure legend, the reader is referred to the web version of this article.)

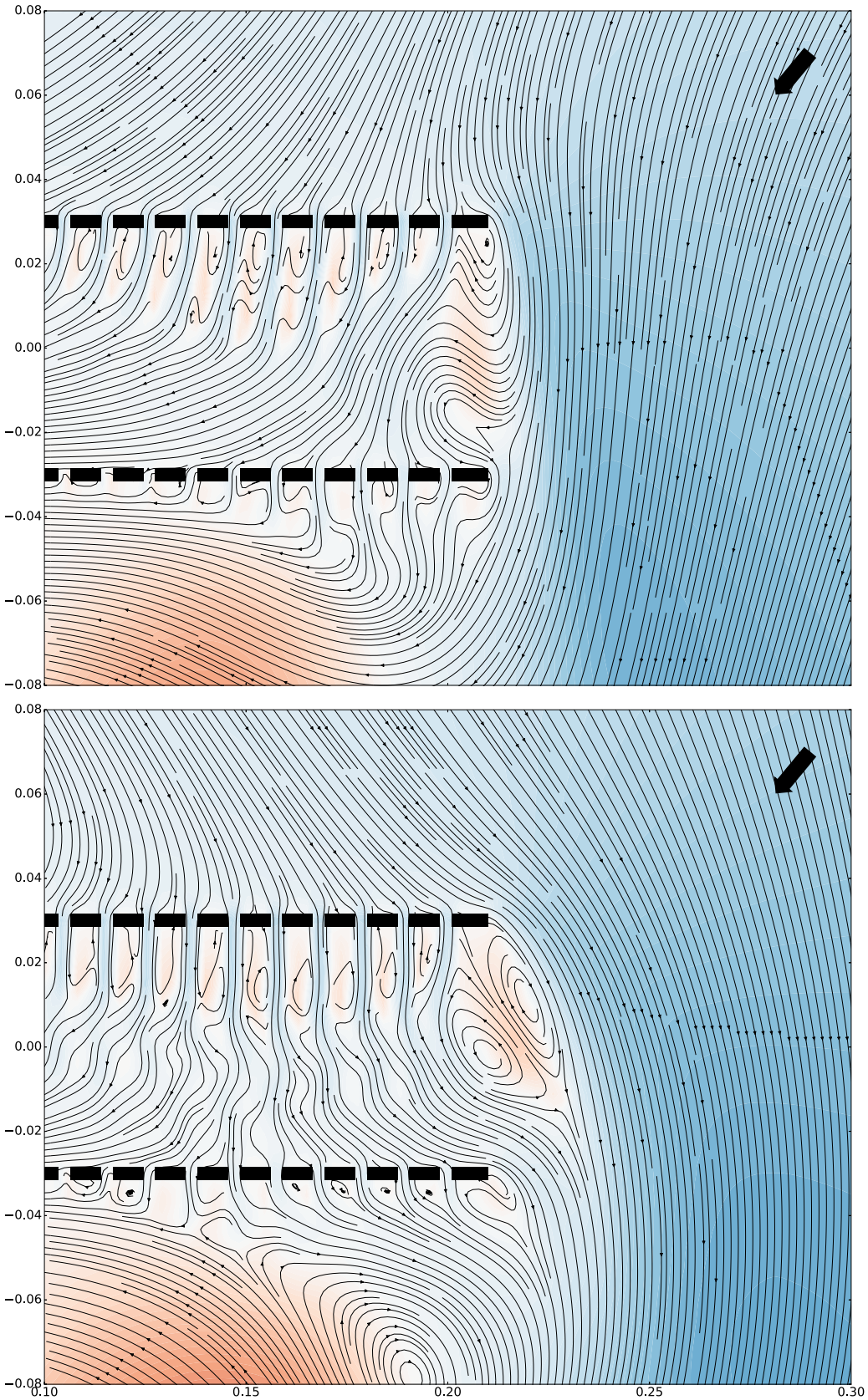

Fig. 23. Flow visualizations zoomed in on the right part of 2P28_60 with orbital flow conditions for KC = 1.95 (top) and KC = 2.05 (bottom). The time-instant is $0.86T$ into an oscillation period ($u = -\frac{D}{T}\mathrm{KC}\cos\omega t$, $w = \frac{D}{T}\mathrm{KC}\sin\omega t$). The color map for the contours represent the vertical velocity (red for positive, blue for negative). (For interpretation of the references to color in this figure legend, the reader is referred to the web version of this article.)

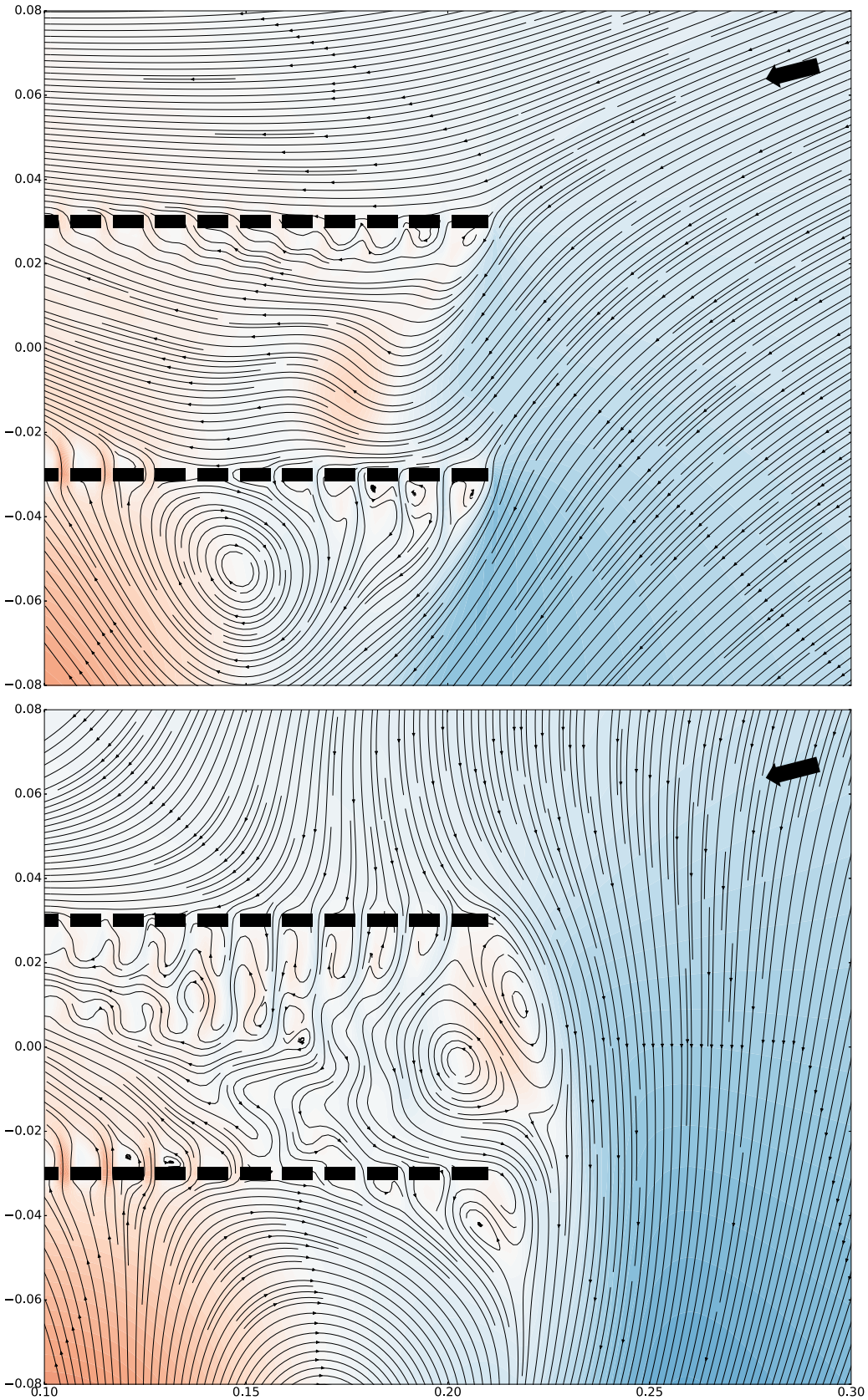

Fig. 24. Flow visualizations zoomed in on the right part of 2P28_60 with orbital flow conditions for KC = 1.95 (top) and KC = 2.05 (bottom). The time-instant is $0.96T$ into an oscillation period ($u = -\frac{D}{T}\mathrm{KC}\cos\omega t$, $w = \frac{D}{T}\mathrm{KC}\sin\omega t$). The color map for the contours represent the vertical velocity (red for positive, blue for negative). (For interpretation of the references to color in this figure legend, the reader is referred to the web version of this article.)

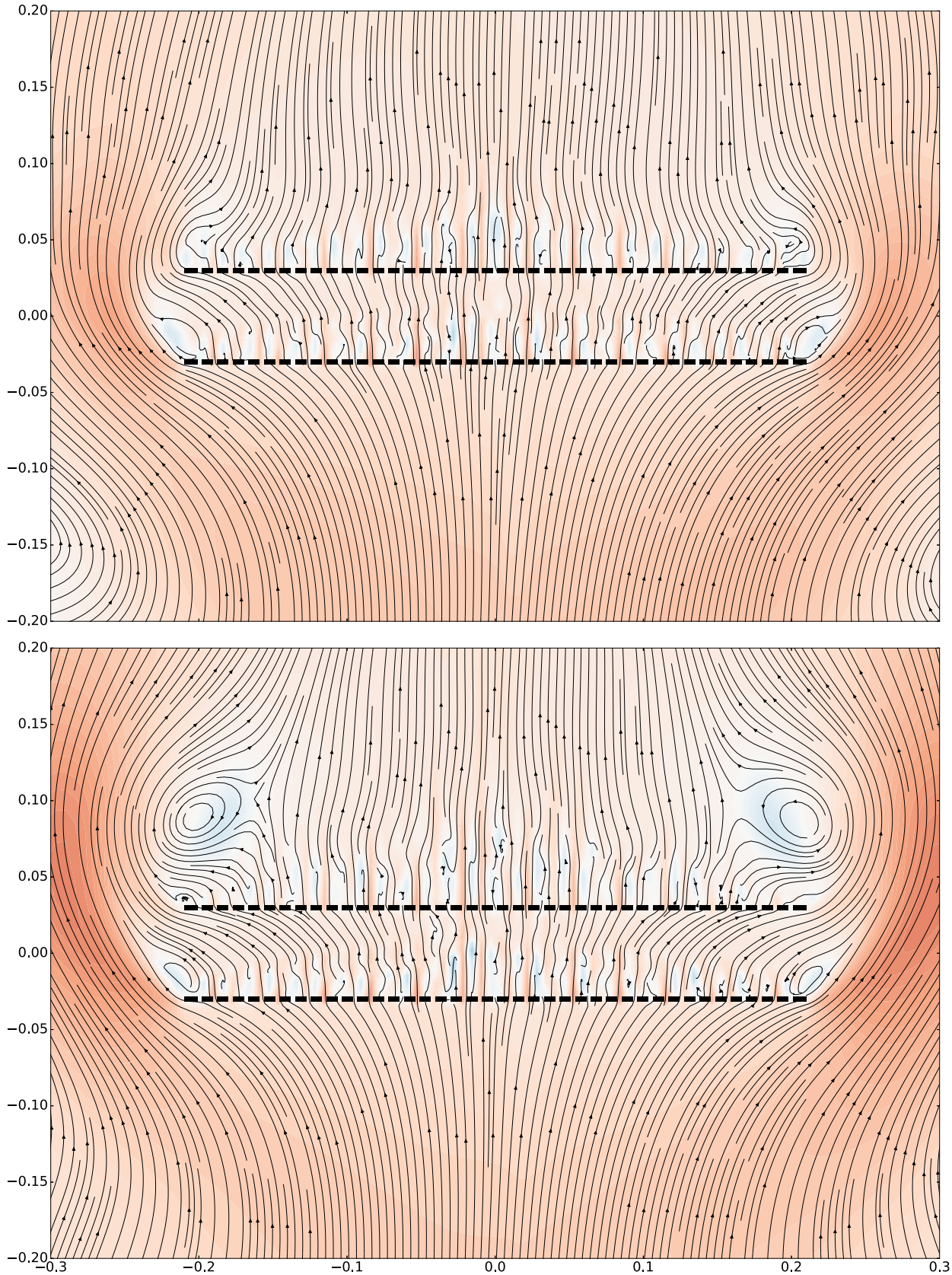

Fig. 25. Flow visualizations of 2P28_60 with oscillating flow conditions for KC = 1.95. The time-instant is $0.12T$ (top) and $0.32T$ (bottom) into an oscillation period ($u = 0$, $w = \frac{D}{T}\mathrm{KC}\sin\omega t$). The color map for the contours represent the vertical velocity (red for positive, blue for negative). (For interpretation of the references to color in this figure legend, the reader is referred to the web version of this article.)

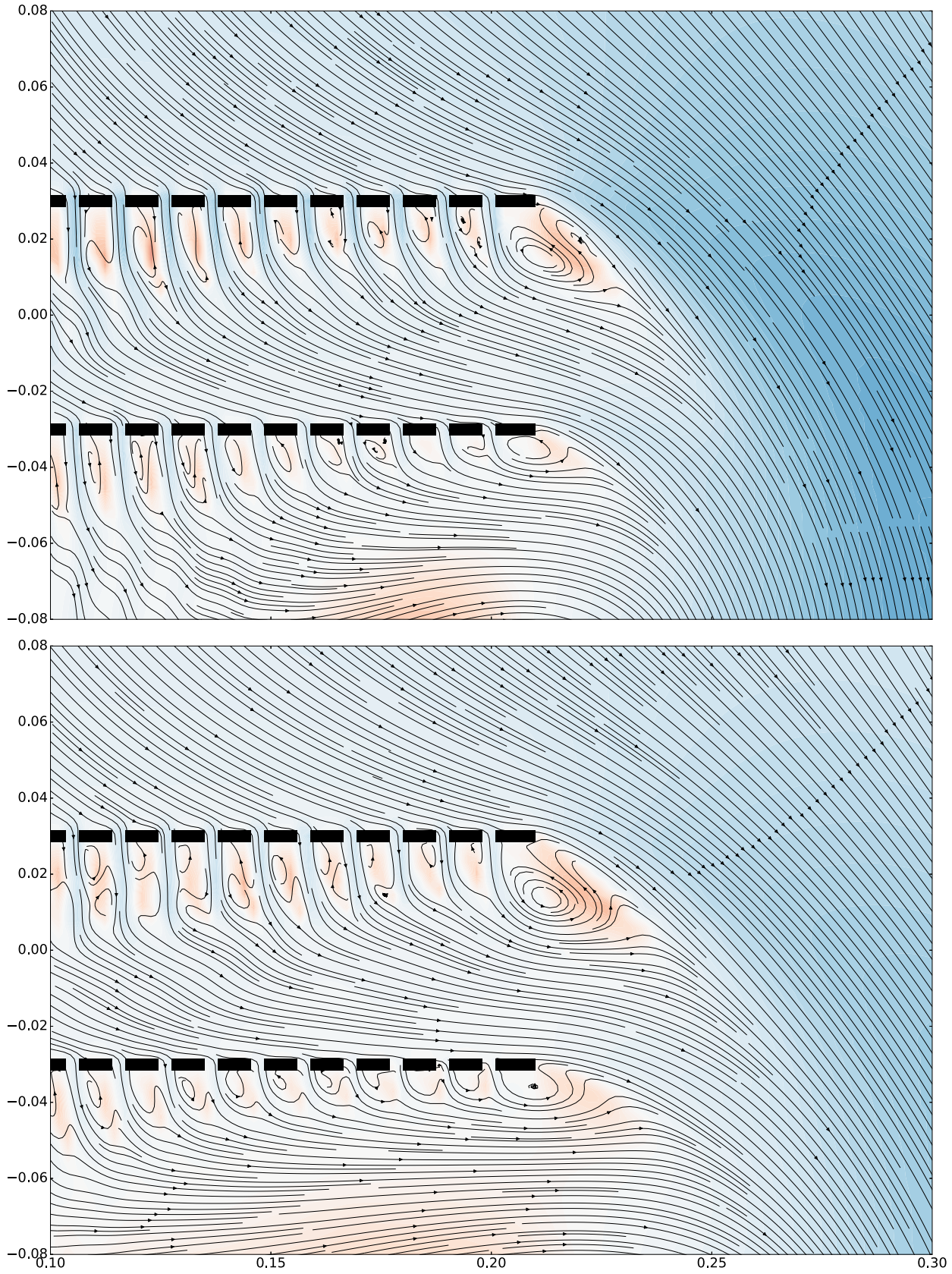

Fig. 26. Flow visualizations zoomed in on the right part of 2P28_60 with oscillating flow conditions for KC = 1.95. The time-instant is $0.76T$ (top) and $0.96T$ (bottom) into an oscillation period ($u = 0$, $w = \frac{D}{T}\mathrm{KC}\sin\omega t$). The color map for the contours represent the vertical velocity (red for positive, blue for negative). (For interpretation of the references to color in this figure legend, the reader is referred to the web version of this article.)

indicates the ambient prescribed flow direction. Despite the small difference in the prescribed velocity, relatively large differences in the flow fields are demonstrated. In particular, the large vortex upstream of the right part of the lower plate, generated during an earlier phase when the vertical velocity was negative, is considerably larger for KC = 2.05 compared to KC = 1.95.

Figs. 20 and 21 show that the vortex ceases to exist at an earlier time instant for KC = 1.95 than for KC = 2.05. In order to investigate the reason for this, flow visualizations of a zoomed-in section of the right part of the plates are presented in Figs. 22–24, for time-instants about one half-cycle prior to those in Figs. 19–21. Both the prescribed vertical and horizontal velocity components are negative at these time-instants, that is, the ambient flow is from upper right to lower left. These time-instants are selected as they illustrate the development of the large vortex below the right part of the lower plate in Figs. 19–21. Flow separation from the right plate-end of the upper plate, and global deflection of the flow, is observed at the first of these time-instants, cf. Fig. 22. As time increases, cf. Fig. 23, and the ambient horizontal velocity increases in magnitude from right to left, the plate-end vortex generated from the upper plate loses its strength in the case of KC = 1.95. Further in time, cf. Fig. 24, flow enters between the two plates from right to left. Contrary, for KC = 2.05, the vortex remains for a longer time, and the flow continues to deflect globally around the whole configuration. The flow visualizations illustrate how slight differences in the flow separation from the right plate-end of the top plate plays a role in global flow behavior; the vortex blocks the flow into the gap. This results in a higher incident velocity on the lower plate, with resulting stronger vortex shedding (as is clearly seen in Fig. 19).

In Figs. 25 and 26, we have included corresponding streamline plots in oscillating flow conditions for KC = 1.95. The streamlines are obtained for time-steps $0.12T$ and $0.32T$ (Fig. 25) and $0.76T$ and $0.96T$ (Fig. 26), corresponding to, respectively, Figs. 19 and 21, and Figs. 22 and 24. The flow field is very symmetric in oscillating flow conditions. The global plate-end vortices in Fig. 25 continue to grow for increasing time-steps before the direction of the prescribed velocity turns at $t = 0.5T$. In Fig. 26, contrary to orbital flow, we observe no inflow between the parallel plates. Instead, the fluid flows through the perforations of the upstream plate and partly through the perforations of the downstream plate, partly out in the gap between the plates.

Large standard deviations, indicating variations in the force between each oscillation cycle, were demonstrated in Figs. 9 and 11 in the hydrodynamic coefficients from orbital flow simulations for large KC numbers, in particular for the added mass coefficient for KC > 2 (2P28_60) and KC > 1.5 (2P28_120). Taking into account the findings from inspection of streamlines in Figs. 19–24, we find it likely that the plate-end flow separation, vortex generation and blocking of the flow into the gap between the plates, which is important for the force on the plates, is highly sensitive to small differences in the flow around these KC numbers, and that this causes the variations in the force.

The large variations in force and coefficients occur for large KC numbers, but for smaller structures these KC numbers can be relevant. However, real sea states are irregular. Steady state does not exist. A practical question is what KC number to choose in a typical industrial study, and how to estimate the force that the structures will be exposed to during a lifting operation. In the first part of the study [1], we found that the force based on coefficients from oscillating flow were conservative compared to orbital flow and incident waves for single perforated plates. These findings are supported for two parallel plates as well, with oscillating flow yielding larger force than those found in orbital conditions, as was demonstrated in for example Fig. 13. Hence, oscillating flow studies have there relevance for force calculations on structures in waves.

How much closer are we thus to reality after studying orbital versus oscillating flow conditions in detail? Well, such a study as the present is the best we can do in order to understand different effects and parameters. In our case we studied oscillating versus orbital flows, as well as gap distance of two plates, and also compared with one plate. We found that varying the gap distance was a factor, and suspect that substructures inside the two plates (equipment on the modules) will be as well. Note that in oscillating flow, we have previously found negligible importance of the substructures [2]. However, substructures may be important for blocking effects and force variations when there is an ambient horizontal velocity component, e.g. in waves. Another issue is how three-dimensional effects will influence the force, in particular with regards to interaction effects as blocking of flow between the two plates. These topics are yet to be solved and are suggested as further work.

6. Conclusion

The hydrodynamic forces and behavior of two-dimensional parallel perforated plate configurations, relevant for several marine applications, were investigated. Forced oscillation experiments and simulations of forced oscillation and orbital flow conditions were performed. Good agreement between experimental and numerical results were found. Therefore, streamline plots were used to study the flow in detail.

Added mass and damping coefficients were presented. The coefficients are functions of amplitude of motion, whereas the period dependence is small. The hydrodynamic force on the structures, which have perforation ratios $\tau = 0.28$, is dominated by damping.

The importance of interaction between the upper and the lower plates of the parallel configurations were discussed. Even at relatively small KC numbers, interaction effects influenced the phase and magnitude of the force on the upper and lower plates in the parallel configurations. In orbital flow, we found that slight differences in the plate-end vortex generation from the upstream plate can give considerable differences in the global flow field and force on the whole structure.

Authors' contribution

This research was carried out in collaboration between both authors.

Fredrik Mentzoni: Carried out the experiments, planned the model tests, carried out the numerical simulations and wrote the manuscript.

Trygve Kristiansen: Participated in planning of model tests and took part in writing the manuscript.

Both authors read and approved the final manuscript.

Declaration of Competing Interest

The authors declare that they have no known competing financial interests or personal relationships that could have appeared to influence the work reported in this paper.

Acknowledgments

This work was financed by the Research Council of Norway, NFR project 237929 CRI MOVE.

References

[1] F. Mentzoni, T. Kristiansen, Two-dimensional experimental and numerical investigations of perforated plates in oscillating flow, orbital flow and incident waves, Manuscript submitted for publication., APOR 2019 662.
[2] F. Mentzoni, M. Abrahamsen-Prsic, T. Kristiansen, Hydrodynamic coefficients of simplified subsea structures, omae2018-78315, Proceedings of the International Conference on Offshore Mechanics and Arctic Engineering, (2018).
[3] F. Mentzoni, T. Kristiansen, Numerical modeling of perforated plates in oscillating flow, Appl. Ocean Res. 84 (2019) 1–11.
[4] F. Mentzoni, T. Kristiansen, A semi-analytical method for calculating the hydrodynamic force on perforated plates in oscillating flow, omae2019-95093, Proceedings of the International Conference on Offshore Mechanics and Arctic Engineering, (2019).
[5] F. Solaas, F. Mentzoni, M. Abrahamsen-Prsic, T. Kristiansen, An experimental and numerical study of added mass and damping for side by side plates in oscillating

flow, omae2019-96008, Proceedings of the International Conference on Offshore Mechanics and Arctic Engineering, (2019).
[6] B. Molin, Hydrodynamic modeling of perforated structures, Appl. Ocean Res. 33 (1) (2011) 1–11.
[7] P.C. Sandvik, F. Solaas, F.G. Nielsen, Hydrodynamic forces on ventilated structures, Proceedings of the International Offshore and Polar Engineering Conference, (2006), pp. 54–58.
[8] L. Tao, D. Dray, Hydrodynamic performance of solid and porous heave plates, Ocean Eng. 35 (10) (2008) 1006–1014.
[9] S. An, O.M. Faltinsen, An experimental and numerical study of heave added mass and damping of horizontally submerged and perforated rectangular plates, J. Fluids Struct. 39 (2013) 87–101.
[10] J. Li, S. Liu, M. Zhao, B. Teng, Experimental investigation of the hydrodynamic characteristics of heave plates using forced oscillation, Ocean Eng. 66 (2013) 82–91.
[11] X. Tian, L. Tao, X. Li, J. Yang, Hydrodynamic coefficients of oscillating flat plates at 0.15 KC 3.15, J. Marine Sci. Technol. 22 (1) (2017) 101–113.
[12] B. Molin, On the added mass and damping of periodic arrays of fully or partially porous disks, J. Fluids Struct. 15 (2) (2001) 275–290.
[13] L. Tao, B. Molin, Y.-M. Scolan, K. Thiagarajan, Spacing effects on hydrodynamics of heave plates on offshore structures, J. Fluids Struct. 23 (8) (2007) 1119–1136.
[14] S. Sudhakar, S. Nallayarasu, Hydrodynamic responses of spar hull with single and double heave plates in random waves, Int. J. Ocean Syst. Eng. 4 (1) (2014) 1–18.
[15] W.W. Jamieson, E.P.D. Mansard, An efficent upright wave absorber, Coastal Hydrodynamics, ASCE, 1987, pp. 124–139.
[16] B. Molin, F. Remy, T. Rippol, Experimental study of the heave added mass and damping of solid and perforated disks close to the free surface, Maritime Industry, Ocean Engineering and Coastal Resources - Proceedings of the 12th International Congress of the International Maritime Association of the Mediterranean, IMAM 2007, 2 (2007), pp. 879–887.
[17] O.M. Faltinsen, Sea Loads on Ships and Offshore Structures, Cambridge Ocean Technology Series, Cambridge University Press, 1993.
[18] A.J. Chorin, Numerical solution of the Navier-Stokes equations, Math. Comput. 22 (104) (1968) 745–762.